ZAMM - Journal of Applied Mathematics and Mechanics

ORIGINAL PAPER OPEN ACCESS

Basins of Attraction and Escape in Pendulum-Type Potentials with Quadratic Air Drag

Attila Genda[1] | Alexander Fidlin[1] | Oleg V. Gendelman[2]

[1]Institute of Engineering Mechanics, Karlsruhe Institute of Technology, Karlsruhe, Germany | [2]Mechanical Engineering, Technion – Israel Institute of Technology, Haifa, Israel

Correspondence: Attila Genda (attila.genda@kit.edu)

Received: 30 March 2026 | **Revised:** 30 March 2026 | **Accepted:** 14 July 2026

Keywords: basin boundary | basin of attraction | dry friction | pendulum | quadratic air drag | quadratic damping | separatrix | washboard potential

ABSTRACT

Quadratic air drag is a common dissipative mechanism at moderate to high velocities, yet in nonlinear one-degree-of-freedom systems, it typically blocks closed-form solutions and energy-based phase-plane partitions. We study the autonomous class

$$\ddot{x} + \alpha(x)\,|\dot{x}|\,\dot{x} + \beta(x)\,\mathrm{sgn}(\dot{x}) + V'(x) = 0,$$

and use a constructive alternative: on trajectory segments with fixed velocity sign, the squared-velocity substitution $p(x) = \dot{x}^2$ converts the dynamics into a first-order linear equation for p as a function of x. This yields explicit phase-plane branches that can be continued and matched across turning points, providing separatrix-type boundaries even when an explicit time parametrization is unavailable.

For the cosine potential, we derive analytic saddle-separatrix branches and provide the critical-velocity thresholds, as well as the winding-number classification of rotations corresponding to each separatrix. Adding dry (Coulomb) friction introduces set-valued dynamics at $\dot{x} = 0$, producing sticking intervals and ribbon-shaped regions of the initial conditions' plane leading to sticking; their boundaries follow from the same branchwise construction for constant, spatially varying, and normal-force-dependent friction laws. For the tilted periodic (washboard) potential $U_F(x) = -\cos x - Fx$, explicit separatrix formulae yield an escape-velocity criterion and a critical damping threshold separating unbounded transport from capture for $|F| < 1$. Analytical boundaries and thresholds are validated against direct time-domain simulations, and the resulting closed and semi-closed expressions provide benchmark cases for numerical basin-boundary and dynamical integrity computations in periodic settings.

MSC2020 Classification: 34C15, 34A34, 37C29, 37N15, 70K44

1 | Introduction

Whenever a mechanical system moves through a surrounding fluid, aerodynamic drag becomes an indispensable part of a realistic model. In many practically important operating ranges, the dissipative force scales approximately with the square of the speed, which is why quadratic drag is routinely adopted in applications ranging from ship roll dynamics and related marine models [1–5] to pendulum experiments and large-amplitude oscillations [6, 7]. Even when fluid mechanics is not modeled explicitly, it is common to represent external losses by a quadratic drag term $D(v) = c_2|v|v$ as a compact dissipative closure that captures the rapid growth of energy loss with speed and often matches measured decay envelopes; see, for example, the energy-balancing identification framework of *Liang* and *Feeny* [8] and a comparison of external damping models in large-deformation settings [9]. At the same time, quadratic drag in oscillatory settings is still less standard in many textbook treatments than linear damping, and specialized laboratory and analysis papers continue to clarify its signatures and parameter identification [10].

In the present paper, we investigate autonomous one-degree-of-freedom motion in a potential under a combination of quadratic air drag and dry (Coulomb) friction,

$$\ddot{x} + \alpha(x)\,|\dot{x}|\,\dot{x} + \beta(x)\,\mathrm{sgn}(\dot{x}) + V'(x) = 0, \qquad \alpha(x) \geq 0,\ \beta(x) \geq 0, \tag{1}$$

interpreted branchwise in the phase plane so that both dissipative terms oppose the motion. The coefficient $\alpha(x)$ may represent effective drag variations with position (geometry, density, projected area), while $\beta(x)$ models Coulomb-type friction, either as a constant level or as an effective spatially varying friction intensity. The presence of $\mathrm{sgn}(\dot{x})$ makes the vector field nonsmooth at $\dot{x} = 0$, but away from rest the dynamics again decomposes naturally into branches with fixed velocity sign.

A key advantage of autonomous 1-DoF dynamics is that the flow can be recast in an energy-displacement form. On any phase-plane branch where the velocity sign is fixed, $\sigma = \mathrm{sgn}(\dot{x})$, we introduce the squared velocity $p(x) = \dot{x}^2$. With this substitution, (1) reduces to a first-order differential equation for p as a function of x; after accounting for σ, the resulting equation is linear on each branch. This representation yields explicit integral formulas and, for many potentials of interest, closed-form or semi-closed-form expressions. Such squared-velocity (or energy-like) descriptions trace back to classical vibration theory and have repeatedly been used to quantify cycle-to-cycle decay and turning-point sequences [11–13], supported by standard asymptotic tools [14–16] as well as later exact and semi-exact treatments covering broad families of restoring forces [17–19]. Modern analytic directions in the same spirit include solvability and integrability results for quadratic-drag oscillators [20–22], as well as non-elementary explicit representations for the classical two-dimensional projectile problem with quadratic air resistance [23–26].

Historically, quadratic resistance in mechanics is closely tied to exterior ballistics and, more generally, to the classical "resisting medium" problem, with the canonical example being planar projectile motion under gravity with a drag force opposing the velocity. In its standard formulation, one considers the coupled 2-DoF dynamics

$$\ddot{\mathbf{r}} = -g\,\mathbf{e}_y - k\,|\dot{\mathbf{r}}|\,\dot{\mathbf{r}}, \qquad \mathbf{r}(t) = (x(t), y(t)), \tag{2}$$

where the dependence on the speed $|\dot{\mathbf{r}}|$ links the horizontal and vertical components, so the motion does not reduce to the kind of 1-DoF phase-plane construction used in the present paper. Models for resisting media go back to Newton's *Principia* [27]. Johann Bernoulli later proposed a hodograph-based approach for quadratic resistance [28], and much of the 18th-century literature developed the ballistic theory further via implicit formulas, series representations, and approximation schemes [29–32], with these developments subsequently summarized in 19th-century treatises such as Didion's monograph [33]. A persistent theme throughout this tradition is that elementary closed-form solutions are rare, and analytical progress typically proceeds through implicit, parametric, or asymptotic descriptions. Early 20th-century accounts continued to catalogue approximations and special configurations [34], while modern historical reviews emphasize how the quadratic-drag projectile problem repeatedly drove the invention and refinement of analytic methods over several centuries [35, 36]. By contrast, we study an autonomous 1-DoF oscillator in a potential well: the branchwise substitution $p(x) = \dot{x}^2$ produces a linear first-order equation on each velocity branch, which in turn permits explicit phase-space trajectory construction.

Despite this substantial body of work, most studies emphasize decay envelopes, frequency corrections, identification of damping laws, forced-response phenomena, or projectile motion. Here, we target a different objective: explicitly determining *basins of attraction* and *escape thresholds*. Concretely, we derive separatrix-type curves in the $(x, \dot{x})$ plane that divide initial conditions according to their long-time outcome. The central question is therefore not how fast the amplitude decays, but to which basin of attraction a given initial condition belongs.

We focus on pendulum-related potentials, in particular the cosine potential and its tilted, spatially periodic variant, the washboard potential. The cosine potential is the standard potential for an angular (phase) variable: it governs the planar pendulum and, more generally, any model with a 2π-periodic, harmonic phase coordinate. Its conservative phase portrait is organized by a separatrix through the unstable equilibrium (the upright position), which divides bounded oscillations (libration within a single well) from rotations (barrier crossing). Under purely viscous-type dissipation, such as quadratic air drag, trajectories generically lose energy and eventually settle at the bottom of a well; approaching the unstable equilibrium is possible only as a limiting separatrix case and therefore has zero probability in the usual sense. Quadratic drag in pendulum motion has been explored experimentally and analytically, including identification from turning-point sequences [7] and closed or semi-closed velocity–angle representations that explicitly exploit the autonomous structure [37]. Instructional studies also discuss the coexistence of quadratic drag with constant-magnitude (Coulomb) friction in oscillatory motion [38]. However, these works primarily describe decay characteristics, whereas the explicit phase-plane partition into distinct asymptotic outcomes is typically not the main output.

Coulomb friction changes the qualitative picture because the friction force has a nonzero magnitude even as $\dot{x} \to 0$ (it switches sign with the velocity and leads to set-valued behavior at $\dot{x} = 0$). In particular, this dry-friction law can create additional terminal behaviors beyond coming to rest in a stable well: depending on the friction level and the approach direction, trajectories may become immobilized either on a finite sticking interval on the $\dot{x} = 0$ axis around the well's bottom, or by sticking near the unstable equilibrium (upright position), once the available driving force from $-V'(x)$ can no longer overcome the friction threshold $\beta(x)$. This makes the cosine potential with Coulomb friction a natural setting in which basins of attraction are genuinely multi-outcome, and in which the boundaries between capture-in-well and sticking-near-top become meaningful objects in their own right.

Tilting the cosine potential produces the washboard potential, a standard model for barrier-crossing and phase-slip phenomena. In superconducting electronics, for example, the resistively and capacitively shunted junction model maps the gauge-invariant phase to an effective particle in a tilted washboard potential [39, 40]. Much of that literature addresses switching statistics, diffusion, parameter identification, or driven response; quadratic damping also appears in more recent Josephson-related studies, often together with forcing [41]. Here, we instead restrict attention to autonomous dynamics and use the squared-velocity reduction to obtain explicit regime maps and the boundaries of safe basins, turning these classical potentials into analytically parameterized benchmark problems for basin geometry and robustness.

Within this framework, we analyze four representative cases:

- cosine potential with pure quadratic air drag ($\beta \equiv 0$),
- cosine potential with Coulomb friction with a constant coefficient ($\beta(x) \equiv \beta_0$),
- cosine potential with Coulomb friction with a spatially varying coefficient (generalization of Equation (1) by allowing $\beta = \beta(x, \dot{x})$),
- washboard potential with pure quadratic air drag ($\beta \equiv 0$).

Across these cases, the objective is the same: derive explicit phase-plane boundaries that separate distinct outcome regions and thereby obtain threshold conditions for capture, sticking, barrier crossing, or runaway motion (where admissible). Related studies do treat escape and basin geometry in dissipative dynamics, but commonly in forced oscillators or in higher-dimensional settings [42, 43], or they focus on existence and classification without delivering explicit basins of attraction boundaries for prescribed potentials [44]. This leaves room for our current study analytically describing the phase-plane partitioning of autonomous 1-DoF systems with pendulum-related potentials under quadratic drag and Coulomb friction. In this sense, we revisit partially classical problems from a complementary viewpoint: not primarily to refine decay laws, but to expose basin geometry and to provide closed, reproducible separatrices.

The analytically obtained boundaries are verified against time-domain simulations. Beyond their intrinsic value, closed or semi-closed basins of attraction boundaries provide useful benchmark test cases for *dynamical integrity* algorithms, where robustness is quantified from the geometry of safe basins [45–48]. Since in practice, integrity measures are typically estimated by gridding or sampling [49], analytically available boundaries offer rare ground truth for evaluating computational procedures, such as the efficient algorithms for the characterization of dynamic integrity of stable equilibria developed in [50, 51].

A closely related constructive approach for autonomous 1-DoF systems with pure quadratic drag (without Coulomb friction), including explicit basin boundaries and dynamic integrity analysis for polynomial potentials (quadratic-cubic potential, double-well Duffing potential, softening quadratic-quartic Duffing potential), is developed in [52].

The remainder of the paper is organized as follows. In Section 2, we derive the branchwise reduction $p(x) = \dot{x}^2$ and obtain the integrating-factor solution for the resulting first-order linear ODE. In Section 3, we apply this construction to the cosine potential, derive explicit basin of attraction boundaries and winding-number (rotation) thresholds, and calculate the local integrity measure (LIM [47]) via a tangency condition together with practical analytic approximations. In Section 4, we include constant Coulomb friction and characterize the resulting sticking bands, sticking ribbons, and the corresponding LIM. In Section 5, we treat normal-force-dependent Coulomb friction, derive a regionwise phase-plane representation with a numerically determined switching point, and compute the LIM over the (α, μ) parameter plane. In Section 6, we study the tilted (washboard) potential, obtain closed-form branch trajectories, and derive the critical damping separating pinned from running motion, including the LIM in the tilted well. Finally, Section 7 summarizes the main findings and outlines directions for future work.

2 | Branchwise Reduction to a first-Order Linear ODE

Consider the autonomous 1-DoF system with quadratic air drag and (optional) Coulomb friction,

$$\ddot{x} + \alpha(x)\,|\dot{x}|\,\dot{x} + \beta(x)\,\operatorname{sgn}(\dot{x}) + V'(x) = 0, \tag{3}$$

where $\alpha(x) \geq 0$ and $\beta(x) \geq 0$ are prescribed, and $V(x)$ is a given potential. A convenient phase-space description is obtained by introducing the squared velocity

$$p(x) := \dot{x}^2 \geq 0, \tag{4}$$

viewed as a function of position along any trajectory segment on which $\dot{x} \neq 0$. On such a segment, the velocity sign

$$\sigma := \operatorname{sgn}(\dot{x}) \in \{+1, -1\} \tag{5}$$

is constant, so that $|\dot{x}|\dot{x} = \sigma\, p$ and $\operatorname{sgn}(\dot{x}) = \sigma$. Moreover,

$$\frac{\mathrm{d}p}{\mathrm{d}x} = \frac{\mathrm{d}(\dot{x}^2)/\mathrm{d}t}{\mathrm{d}x/\mathrm{d}t} = \frac{2\dot{x}\ddot{x}}{\dot{x}} = 2\ddot{x}, \qquad (\dot{x} \neq 0), \tag{6}$$

and substituting $\ddot{x} = \frac{1}{2}\,\mathrm{d}p/\mathrm{d}x$ into (1) yields, on each fixed-σ branch, the linear first-order ODE

$$\frac{\mathrm{d}p}{\mathrm{d}x} + 2\sigma\,\alpha(x)\,p = -2V'(x) - 2\sigma\,\beta(x). \tag{7}$$

Thus, for prescribed $\alpha(x)$, $\beta(x)$, and $V(x)$, the phase trajectories are obtained by solving Equation (7) separately for $\sigma = \pm 1$ and reconstructing the velocity as

$$\dot{x} = \sigma\sqrt{p(x)} \qquad \text{on intervals where } p(x) \geq 0. \tag{8}$$

Turning points correspond to $p = 0$, where $\dot{x}$ changes sign and the governing branch switches; the global motion is formed by concatenating the corresponding local solutions.

2.1 | Integrating-Factor Form

Introducing the integrating factor

$$\mu_\sigma(x) = \exp\left(2\sigma \int_{x_*}^{x} \alpha(\xi)\,\mathrm{d}\xi\right), \tag{9}$$

Equation (7) can be written as

$$\frac{\mathrm{d}}{\mathrm{d}x}\big(p(x)\mu_\sigma(x)\big) = -2\big(V'(x) + \sigma\beta(x)\big)\mu_\sigma(x). \tag{10}$$

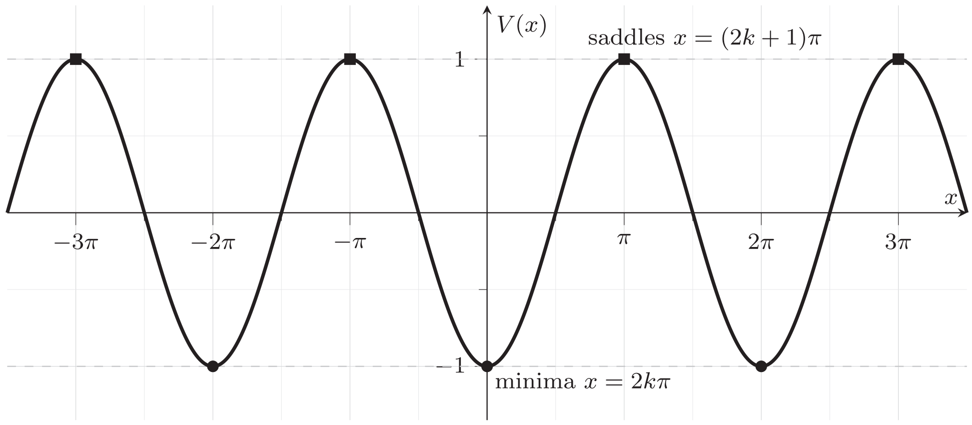

FIGURE 1 | Periodic potential $V(x) = -\cos x$ with saddles at $(2k+1)\pi$.

Therefore, for a reference point (x_0, v_0) with $v_0 \neq 0$ and $\sigma = \mathrm{sgn}(v_0)$,

$$p_\sigma(x) = \frac{1}{\mu_\sigma(x)} \left[v_0^2 \mu_\sigma(x_0) - 2 \int_{x_0}^{x} \big(V'(s) + \sigma\beta(s) \big) \mu_\sigma(s)\,\mathrm{d}s \right]. \tag{11}$$

This representation is exact and requires only a single quadrature once α and β are specified; where the integral can be evaluated in closed form, it yields explicit analytic phase-plane curves.

3 | Cosine Potential

3.1 | Model, Equilibria, and Branchwise Reduction

Consider the 2π-periodic potential, depicted in Figure 1

$$V(x) = -\cos x, \qquad V'(x) = \sin x, \tag{12}$$

together with the autonomous equation of motion

$$\ddot{x} + \alpha\,|\dot{x}|\,\dot{x} + V'(x) = 0, \qquad \alpha > 0. \tag{13}$$

In the conservative limit $\alpha = 0$, this reduces to the classical pendulum equation. The equilibria consist of the minima $x_{m,k} = 2k\pi$ and the saddles $x_{s,k} = (2k+1)\pi$, $k \in \mathbb{Z}$. The phase portrait inherits the spatial periodicity, so it suffices to study the reference cell around $x_{m,0} = 0$ and its neighboring saddles at $\pm\pi$.

To obtain explicit phase trajectories, we apply the squared-velocity substitution $p(x) = \dot{x}^2$ on any phase-plane branch with fixed velocity sign $\sigma = \mathrm{sgn}(\dot{x}) \in \{+1, -1\}$. As summarized in Section 2, this transforms Equation (13) into a first-order linear equation for p on each fixed-sign branch,

$$\frac{\mathrm{d}p}{\mathrm{d}x} + 2\alpha\sigma\,p = -2\sin x, \qquad p(x) = \dot{x}^2, \tag{14}$$

which should be interpreted only on intervals where the sign σ remains constant. Using the integrating factor $\mu_\sigma(x) = e^{2\alpha\sigma x}$, the trajectory passing through (x_0, v_0) with $v_0 \neq 0$ admits the exact integral representation

$$p_\sigma(x; x_0, v_0) = e^{-2\alpha\sigma x} \left[v_0^2 e^{2\alpha\sigma x_0} - 2 \int_{x_0}^{x} \sin s\, e^{2\alpha\sigma s}\,\mathrm{d}s \right]. \tag{15}$$

Evaluating the integral yields the closed form

$$p_\sigma(x; x_0, v_0) = A_\sigma^{(0)}(x) + e^{-2\alpha\sigma(x-x_0)}\left[v_0^2 - A_\sigma^{(0)}(x_0)\right], \tag{16}$$

where

$$A_\sigma^{(0)}(x) := \frac{2}{4\alpha^2+1}(\cos x - 2\alpha\sigma\sin x). \tag{17}$$

On any interval where $p_\sigma(x) \geq 0$, the corresponding phase-plane branch is given by $\dot{x} = \sigma\sqrt{p_\sigma(x)}$.

3.2 | Basin of Attraction Boundaries and Winding-Number Classification

We now translate the explicit branchwise formula into basin-of-attraction boundaries. Fix the reference well around $x_{m,0} = 0$ and consider rightward transport towards the neighboring saddle $x_{s,0} = \pi$. The boundary separating trajectories that remain captured in the reference well from those that cross into the next well is characterized by a critical orbit that reaches the saddle with zero velocity. Since the approach to π is right-going, this boundary is defined by

$$p_+(\pi; x_0, v_0) = 0, \qquad x_0 \in (-\infty, \pi), \tag{18}$$

where the subscript $+$ indicates the branch $\sigma = +1$. Substituting Equation (16) and solving for the launch velocity gives

$$\begin{aligned} v_{\text{crit}}^2(x_0;\alpha) &= A_+^{(0)}(x_0) - e^{2\alpha(\pi-x_0)}A_+^{(0)}(\pi) \\ &= \frac{2}{4\alpha^2+1}\left(\cos x_0 - 2\alpha\sin x_0 + e^{2\alpha(\pi-x_0)}\right), \qquad x_0 \in (-\infty,\pi), \end{aligned} \tag{19}$$

and therefore the right boundary branch in the $(x, \dot{x})$ plane becomes

$$\dot{x} = +\sqrt{v_{\text{crit}}^2(x;\alpha)}. \tag{20}$$

The left boundary follows analogously by symmetry.

For transport across multiple wells, it is natural to classify trajectories by the number of crossed saddles $x_{s,n} = (2n+1)\pi$, $n \geq 0$. The threshold for reaching $x_{s,n}$ with zero velocity is again obtained by imposing $p_+(x_{s,n}; x_0, v_0) = 0$. This yields the integral form

$$v_{\text{crit},n}^2(x_0;\alpha) = e^{-2\alpha x_0}J_+(x_{s,n}; x_0), \qquad J_+(x;x_0) := 2\int_{x_0}^{x}\sin s\, e^{2\alpha s}\,\mathrm{d}s, \qquad n = 0,1,2,\ldots \tag{21}$$

and, using Equation (17), the closed form

$$v_{\text{crit},n}^2(x_0;\alpha) = A_+^{(0)}(x_0) - e^{2\alpha(x_{s,n}-x_0)}A_+^{(0)}(x_{s,n}) = \frac{2}{4\alpha^2+1}\left(\cos x_0 - 2\alpha\sin x_0 + e^{2\alpha(x_{s,n}-x_0)}\right). \tag{22}$$

Accordingly, the winding number (number of completed rotations) is determined by the stripe condition

$$N = \#\left\{n \geq 0 :\ v_0^2 \geq v_{\text{crit},n}^2(x_0;\alpha)\right\}. \tag{23}$$

The critical velocities $v_{\text{crit},n}(x_0; \alpha = 0.05)$, which are also basin boundaries at the same time, are shown in Figure 2 for $\alpha = 0.05$. The critical velocities $v_{\text{crit},n}(x_0 = 2k\pi; \alpha)$ for rotations started at the bottom of the well, are shown in Figure 3 for the range of $\alpha = [0, 0.1]$.

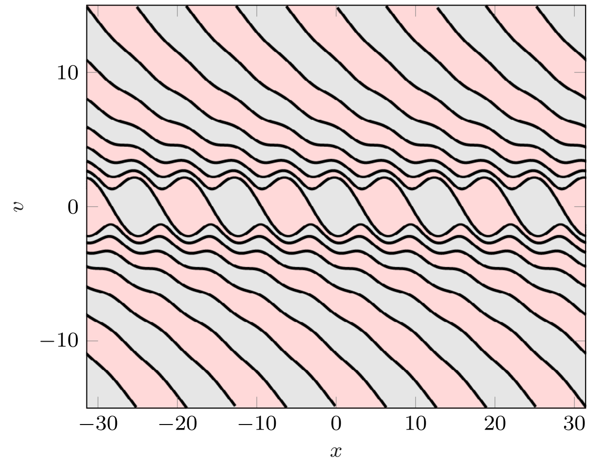

FIGURE 2 | Analytical basin-of-attraction boundary for $V(x) = -\cos x$ with quadratic drag, compared to time-domain simulations for $\alpha = 0.05$.

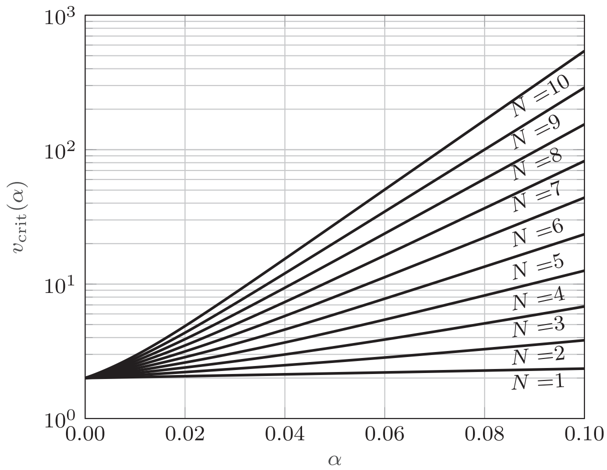

FIGURE 3 | Critical velocities for N complete rotations as a function of α for motion starting at $x_0 = 2k\pi$.

3.3 | Local Integrity Measure of the Equilibrium at the Origin

The LIM associated with the attractor at $(0, 0)$ is defined as the largest radius $r_{\mathrm{loc}}(\alpha)$ for which the closed disk $x^2 + \dot{x}^2 \leq r_{\mathrm{loc}}^2$ lies entirely inside the basin of attraction of $(0, 0)$. Equivalently, $r_{\mathrm{loc}}(\alpha)$ is the minimum Euclidean distance from the origin to the basin boundary. For the cosine potential, this boundary is given by the saddle separatrix passing through $x = \pi$, that is, the branch satisfying $p(\pi) = 0$. To measure this distance, it is convenient to describe the relevant separatrix segment in polar coordinates centered at the origin,

$$x = r\cos\theta, \qquad \dot{x} = r\sin\theta, \qquad r \geq 0, \tag{24}$$

and focus on the upper-right portion of the basin boundary ($\dot{x} \geq 0$) that approaches the saddle at $x = \pi$. Along this separatrix, one may write

$$\dot{x} = +\sqrt{p_+(x;\pi,0)}, \qquad x \in [0, \pi], \tag{25}$$

where $p_+(x;\pi,0)$ denotes the $\sigma = +1$ solution of Equation (14) with the saddle condition $p(\pi) = 0$. Using Equation (16) with $x_0 = \pi$ and $v_0 = 0$ yields the explicit phase trajectory

$$p_+(x;\pi,0) = \frac{2}{4\alpha^2 + 1}\left(\cos x - 2\alpha\sin x + e^{2\alpha(\pi - x)}\right), \qquad p_+(\pi;\pi,0) = 0. \tag{26}$$

Consequently, the separatrix admits the polar parametrization

$$r(x) = \sqrt{x^2 + p_+(x;\pi,0)}, \qquad \theta(x) = \operatorname{atan2}\Big(\sqrt{p_+(x;\pi,0)},\ x\Big), \tag{27}$$

and, equivalently, the implicit polar relation

$$r(\theta)^2 \sin^2\theta = p_+(r(\theta)\cos\theta;\pi,0), \qquad \theta \in [0,\pi/2]. \tag{28}$$

The LIM is the minimum radius attained along this boundary,

$$r_{\mathrm{loc}}(\alpha) = \min r(\theta) = \min_{x\in[0,\pi]} r(x) = \min_{x\in[0,\pi]} \sqrt{x^2 + p_+(x;\pi,0)}. \tag{29}$$

Since

$$\frac{\mathrm{d}}{\mathrm{d}x}\Big(x^2 + p_+(x;\pi,0)\Big)\Big|_{x=0} = p_+'(0;\pi,0) = \frac{2}{4\alpha^2+1}\Big(-2\alpha - 2\alpha e^{2\alpha\pi}\Big) < 0 \tag{30}$$

and

$$\frac{\mathrm{d}}{\mathrm{d}x}\Big(x^2 + p_+(x;\pi,0)\Big)\Big|_{x=\pi} = 2\pi + p_+'(\pi;\pi,0) = 2\pi > 0, \tag{31}$$

the minimizer occurs at an interior tangency point $x = x_{\mathrm{int}}(\alpha) \in (0,\pi)$ determined by stationarity of $r^2(x)$,

$$\frac{\mathrm{d}}{\mathrm{d}x}\big(x^2 + p_+(x;\pi,0)\big) = 0 \quad\Longleftrightarrow\quad 2x + p_+'(x;\pi,0) = 0. \tag{32}$$

Using the branch Equation (14) for $\sigma = +1$, $p_+'(x;\pi,0) + 2\alpha\, p_+(x;\pi,0) = -2\sin x$, the stationarity condition becomes

$$x = \alpha\, p_+(x;\pi,0) + \sin x. \tag{33}$$

Substituting Equation (26) yields the explicit transcendental equation for $x_{\mathrm{int}}(\alpha)$,

$$(4\alpha^2+1)\,x = \sin x + 2\alpha\cos x + 2\alpha\, e^{2\alpha(\pi-x)}, \qquad x \in (0,\pi). \tag{34}$$

Moreover, defining

$$F(x) := (4\alpha^2+1)\,x - \sin x - 2\alpha\cos x - 2\alpha e^{2\alpha(\pi-x)}, \tag{35}$$

one finds

$$F'(x) = 4\alpha^2 + 1 - \cos x + 2\alpha\sin x + 4\alpha^2 e^{2\alpha(\pi-x)} > 0, \qquad x \in [0,\pi], \tag{36}$$

so Equation (34) possesses a unique solution in $(0,\pi)$. Finally, the LIM follows from the minimizing point $x_{\mathrm{int}}(\alpha)$ as

$$r_{\mathrm{loc}}(\alpha) = \sqrt{x_{\mathrm{int}}(\alpha)^2 + p_+(x_{\mathrm{int}}(\alpha);\pi,0)}, \tag{37}$$

where $x_{\mathrm{int}}(\alpha) \in (0,\pi)$ is the unique solution of the tangency Equation (34).

Closed-form solutions are not available for Equation (34); however, analytic approximations can be obtained. We summarize four practical options that cover the regimes $\alpha \to 0^+$ and $\alpha \to \infty$, and provide convenient closed expressions for intermediate α.

(i) *Small-α expansion*. As $\alpha \to 0^+$, the tangency point satisfies $x_{\mathrm{int}}(\alpha) \to 0$. Subtracting x from both sides of Equation (34) gives

$$x - \sin x = 2\alpha\cos x + 2\alpha e^{2\alpha(\pi-x)} - 4\alpha^2 x, \tag{38}$$

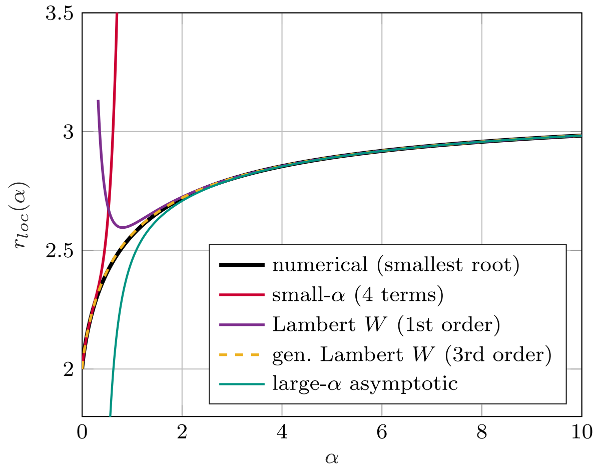

FIGURE 4 | Numerically calculated LIM ($r_{\text{loc}}(\alpha)$) versus different approximations.

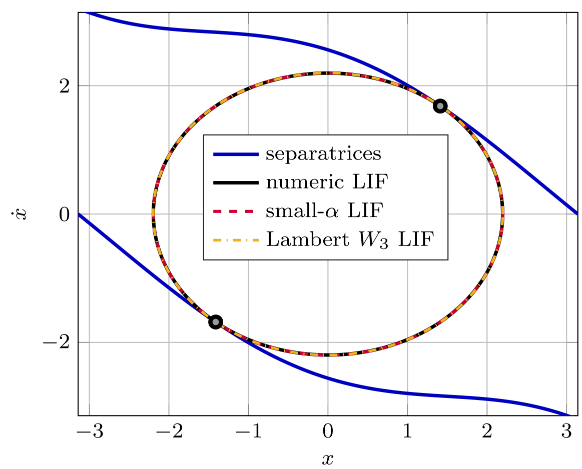

FIGURE 5 | Phase-plane separatrices for $\alpha = 0.15$ and LIM circles (centered at the origin): $r_{\text{loc}}^{\text{num}} = 2.19618$, $r_{\text{loc}}^{\text{s}-\alpha} = 2.19685$, $r_{\text{loc}}^{\text{3W}} = 2.19708$.

so the dominant balance is $x - \sin x \sim x^3/6$ against the $O(\alpha)$ forcing $2\alpha \cos x + 2\alpha e^{2\alpha(\pi - x)} \sim 4\alpha$, which implies $x_{\text{int}}(\alpha) = O(\alpha^{1/3})$. Accordingly, introduce $\varepsilon = \alpha^{1/3}$ and seek a Puiseux-type expansion

$$x_{\text{int}}(\alpha) = A\varepsilon + B\varepsilon^3 + C\varepsilon^4 + D\varepsilon^5 + O(\varepsilon^6) \quad \left(\varepsilon^3 = \alpha\right), \tag{39}$$

and insert this ansatz together with the Taylor series of $\sin x$, $\cos x$, and the exponential factor $e^{2\alpha(\pi - x)}$ into Equation (34). Matching coefficients order by order yields

$$x_{\text{int}}(\alpha) = (24\alpha)^{1/3} - \frac{8}{5}\alpha + \frac{8\pi}{24^{2/3}}\alpha^{4/3} - \frac{169}{350}24^{2/3}\alpha^{5/3} + O(\alpha^2), \qquad \alpha \to 0^+. \tag{40}$$

In computations, the corresponding small-α approximation for the LIM is obtained by evaluating the exact separatrix formula (26) at $x_{\text{sa}}(\alpha)$ from Equation (40) and then inserting into Equation (37), that is,

$$r_{\text{loc}}(\alpha) \approx \sqrt{x_{\text{sa}}(\alpha)^2 + p_+(x_{\text{sa}}(\alpha); \pi, 0)}. \tag{41}$$

This keeps the small-α asymptotics in the minimizing location, while avoiding an additional truncation error in p_+. The small-α approximation Equation (40) is depicted in Figure 4. For $\alpha = 0.15$, the corresponding LIM value shows exact agreement up to visualization accuracy (cf. Figure 5).

(ii) *First-order Lambert-W approximation*. Replacing $\sin x \approx x$ and $\cos x \approx 1$ in Equation (34) gives $(2\alpha x - 1)e^{2\alpha x} = e^{2\alpha\pi}$, hence

$$x_{\text{int}}(\alpha) \approx x_W(\alpha) := \frac{1 + W_0\left(e^{2\alpha\pi - 1}\right)}{2\alpha}, \qquad \alpha > 0, \tag{42}$$

where W_0 denotes the principal branch of the Lambert W function. The associated LIM approximation is again obtained from Equation (37) by inserting $x_W(\alpha)$. This approximation is mainly useful for moderate and large α; for sufficiently small α, it may fall outside the physically relevant interval $x \in (0, \pi)$.

(iii) *Third-order truncation and generalized Lambert W*. Using $\sin x \approx x - \frac{x^3}{6}$ and $\cos x \approx 1 - \frac{x^2}{2}$ in Equation (34) yields the polynomial-exponential equation

$$\left(u^3 + 12\alpha^2 u^2 + 96\alpha^4 u - 96\alpha^4\right)e^u = 96\alpha^4 e^{2\alpha\pi}, \qquad u := 2\alpha x. \tag{43}$$

Let $u_1(\alpha), u_2(\alpha), u_3(\alpha)$ denote the roots of the cubic in Equation (43). Then, Equation (43) can be written in the canonical form $e^u \prod_{j=1}^{3}(u - u_j) = 96\alpha^4 e^{2\alpha\pi}$, so that u can be represented by the generalized Lambert-W function in the sense of *Mezö* and *Baricz* [53, 54],

$$u \approx W\left(u_1(\alpha), u_2(\alpha), u_3(\alpha);\, 96\alpha^4 e^{2\alpha\pi}\right), \qquad x_{\text{int}}(\alpha) \approx x_{\text{gW}}(\alpha) := \frac{u}{2\alpha}. \tag{44}$$

The physically relevant approximation corresponds to the smallest positive real solution $x_{\text{gW}}(\alpha) \in (0, \pi)$, and $r_{\text{loc}}(\alpha)$ follows from Equation (37).

(iv) *Large-α asymptotics*. To derive an explicit asymptotic expansion for the tangency point, we set $x_{\text{int}}(\alpha) = \pi - \delta(\alpha)$ with $0 < \delta \ll 1$ and introduce the stretched variable

$$u := 2\alpha\,\delta. \tag{45}$$

Using $\sin(\pi - \delta) = \sin\delta$, $\cos(\pi - \delta) = -\cos\delta$, and the Taylor expansions

$$\sin\delta = \delta - \frac{\delta^3}{6} + O(\delta^5), \qquad \cos\delta = 1 - \frac{\delta^2}{2} + O(\delta^4), \tag{46}$$

the tangency Equation (34) can be rewritten as

$$e^u = 2\pi\alpha - u + 1 + \frac{\pi}{2\alpha} + O\left(\frac{(\ln\alpha)^2}{\alpha^2}\right), \qquad \alpha \to \infty, \tag{47}$$

where $u = O(\ln\alpha)$ has been used. Writing $L := \ln(2\pi\alpha)$ and solving Equation (47) by logarithmic iteration yields the expansion

$$u = L + \frac{1 - L}{2\pi\alpha} + \frac{\pi^2 + (L-1) - \frac{1}{2}(L-1)^2}{(2\pi\alpha)^2} + O\left(\frac{(\ln\alpha)^3}{\alpha^3}\right), \qquad \alpha \to \infty. \tag{48}$$

Since $\delta = u/(2\alpha)$, this gives

$$x_{\text{int}}(\alpha) = \pi - \frac{L}{2\alpha} + \frac{L-1}{4\pi\alpha^2} - \frac{1}{8\alpha^3} + \frac{(L-1)^2}{16\pi^2\alpha^3} - \frac{L-1}{8\pi^2\alpha^3} + O\left(\frac{(\ln\alpha)^3}{\alpha^4}\right), \qquad L = \ln(2\pi\alpha). \tag{49}$$

For the LIM, one has $r_{\text{loc}}(\alpha) = \sqrt{x_{\text{int}}^2 + p_+(x_{\text{int}}; \pi, 0)}$. Using the closed-form expression of p_+ for the cosine potential (and constant α) and expanding at $x_{\text{int}} = \pi - \delta$ gives $p_+(x_{\text{int}}; \pi, 0) = \pi/\alpha - u/\alpha^2 + O((\ln\alpha)^2/\alpha^3)$. A consistent Taylor expansion of the square root then yields

$$r_{\text{loc}}(\alpha) = \pi + \frac{1 - L}{2\alpha} - \frac{3}{8\pi\alpha^2} - \frac{1}{8\alpha^3} + \frac{2 - L - L^2}{16\pi^2\alpha^3} + O\left(\frac{(\ln\alpha)^3}{\alpha^4}\right), \qquad L = \ln(2\pi\alpha). \tag{50}$$

4 | Cosine Potential with Constant Coulomb Friction

4.1 | Model and Branchwise Phase-Plane Representation

We now supplement quadratic air drag by a constant Coulomb friction level. This is a standard idealization for pendulum-type devices in which aerodynamic drag dominates at moderate and large angular velocities (well described by a quadratic law), while the bearing contributes an approximately constant resisting torque. The coexistence of quadratic drag and dry friction in oscillatory motion, and its influence on decay and turning-point sequences, is discussed, for example, in [7, 38], and explicit velocity-angle representations for quadratic drag that exploit the autonomous structure are given in [37]. In addition, the normal force in the bearing contains a centrifugal contribution proportional to $\dot{x}^2$, so even a nominal Coulomb mechanism can acquire an effective speed dependence at high velocities. First, we intentionally keep the friction magnitude constant, $\beta(x) \equiv \beta \geq 0$, to isolate the nonsmooth sticking effect and its impact on the partition of basins of attraction and integrity measures.

Accordingly, we consider the cosine potential $V(x) = -\cos x$ and the autonomous dynamics

$$\ddot{x} + \alpha|\dot{x}|\,\dot{x} + \beta\,\operatorname{sgn}(\dot{x}) + \sin x = 0, \qquad \alpha > 0,\ \beta \geq 0. \tag{51}$$

On any trajectory segment with fixed velocity sign $\sigma = \operatorname{sgn}(\dot{x}) \in \{+1, -1\}$, introduce the squared velocity $p(x) = \dot{x}^2$. Then, (51) reduces to the linear first-order ODE

$$\frac{\mathrm{d}p}{\mathrm{d}x} + 2\alpha\sigma\,p = -2\sin x - 2\beta\sigma, \qquad p(x) = \dot{x}^2, \tag{52}$$

valid away from rest ($\dot{x} \neq 0$). With integrating factor $\mu_\sigma(x) = e^{2\alpha\sigma x}$, the trajectory through (x_0, v_0), $v_0 \neq 0$ admits the closed form

$$p_\sigma(x; x_0, v_0) = A_\sigma(x) + e^{-2\alpha\sigma(x-x_0)}\big[v_0^2 - A_\sigma(x_0)\big], \tag{53}$$

where

$$A_\sigma(x) := \frac{2}{4\alpha^2+1}(\cos x - 2\alpha\sigma\sin x) - \frac{\beta}{\alpha}. \tag{54}$$

On intervals where $p_\sigma(x) \geq 0$, the velocity is $\dot{x} = \sigma\sqrt{p_\sigma(x)}$. Turning points satisfy $p_\sigma = 0$ and trigger a branch switch.

4.2 | Basins of Attraction, Rotations, and Sticking Ribbons

The saddle points remain at $x_{s,n} = (2n+1)\pi$. For right-going initial motion ($v_0 > 0$) starting in the reference cell $x_0 \in (-\pi, \pi)$, the critical condition for reaching the saddle $x_{s,n}$ with zero velocity is $p_+(x_{s,n}; x_0, v_0) = 0$, which gives

$$v^2_{\mathrm{crit},n}(x_0) = A_+(x_0) - e^{2\alpha(x_{s,n}-x_0)}A_+(x_{s,n}), \qquad n = 0, 1, 2, \ldots, \tag{55}$$

with $A_+(x)$ from Equation (54). As in the purely quadratic case, these curves form ordered "stripes" and determine the rotation count via

$$N = \#\Big\{n \geq 0 :\ v_0^2 \geq v^2_{\mathrm{crit},n}(x_0)\Big\}. \tag{56}$$

Figures 6 and 7 compare the analytically constructed boundaries (dashed lines) with time-domain simulations (colored areas).

A qualitative novelty is sticking. At $\dot{x} = 0$, the friction term is set-valued, and a static equilibrium is admissible whenever the restoring torque can be balanced by a friction force of magnitude at most β, that is,

$$|\sin x| \leq \beta. \tag{57}$$

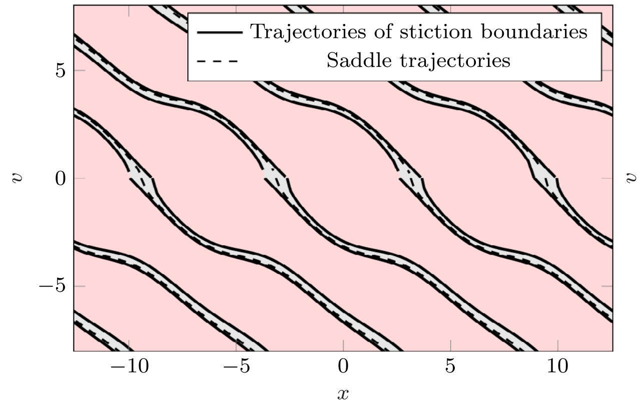

FIGURE 6 | Ribbon-shaped domains of the phase space that correspond to a pendulum motion stopping around the upper equilibrium position for $\alpha = 0.05$ and $\beta = 0.5$.

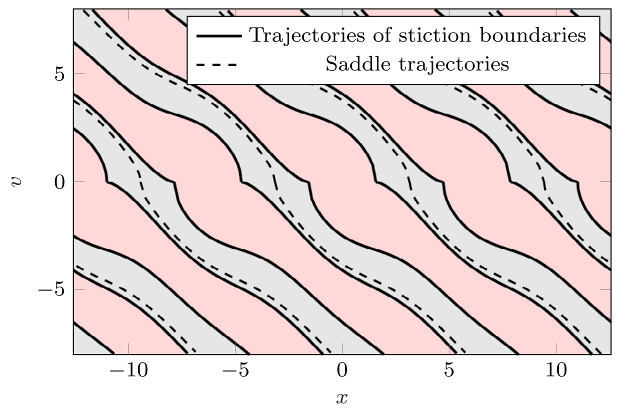

FIGURE 7 | Ribbon-shaped domains of the phase space that correspond to a pendulum motion stopping around the upper equilibrium position for $\alpha = 0.05$ and $\beta = 1$.

Around the saddle $x_s = \pi$, this defines a sticking interval

$$x_{s,-} \leq x \leq x_{s,+}, \qquad x_{s,\pm} := \pi \pm \delta_s, \qquad \delta_s := \arcsin \beta, \qquad 0 \leq \beta \leq 1. \tag{58}$$

The phase portrait, therefore, contains ribbon-shaped sets of initial conditions whose first turning point falls inside $[x_{s,-}, x_{s,+}]$, after which the motion terminates in a stuck state near the top. For the upper-right quadrant ($x \geq 0$, $\dot{x} \geq 0$), the relevant ribbon boundary is obtained by requiring that the first turning point equals the left endpoint

$$x_T := x_{s,-} = \pi - \delta_s. \tag{59}$$

Using Equation (53) with $\sigma = +1$ and imposing $p_{\mathrm{rib}}(x) := p_+(x_T; x, 0) = 0$ yields the boundary graph

$$\dot{x} = +\sqrt{p_{\mathrm{rib}}(x)}, \qquad p_{\mathrm{rib}}(x) := A_+(x) - e^{2\alpha(x_T - x)} A_+(x_T), \qquad x \in [0, x_T], \tag{60}$$

where $A_+(x)$ is given by Equation (54). We remind ourselves that $p_{\mathrm{rib}}(x; \alpha, \beta)$ also depends on the parameters α and β, but for simplicity, we do not write them out unless necessary. Figures 6 and 7 illustrate these sticking ribbons for two friction levels (continuous lines).

4.3 | LIM Determined by the Sticking-Ribbon Boundary

We now extend the LIM construction of Section 3.3 to Equation (51). The LIM of the attractor at (0,0) is the largest radius $r_{\text{loc}}(\alpha,\beta)$ such that the closed disk $x^2+\dot{x}^2 \le r_{\text{loc}}^2$ lies entirely inside the basin of attraction of (0,0), equivalently, the minimum Euclidean distance from the origin to the basin boundary.

For $\beta > 0$, the closest obstruction to attraction at (0,0) is the onset of sticking near the neighbouring saddle at $x=\pi$: initial conditions that lie above the upper-right ribbon boundary (60) can reach the saddle neighborhood with the first turning point inside $[x_{s,-}, x_{s,+}]$ and then terminate in a stuck state near the top. Consequently, the LIM of (0,0) is determined by the distance from the origin to the ribbon boundary (60). We define the radial distance along the ribbon boundary by

$$r(x) := \sqrt{x^2 + p_{\text{rib}}(x)}, \qquad x \in [0, x_T], \tag{61}$$

with p_{rib} from Equation (60). Then

$$r_{\text{loc}}(\alpha,\beta) = \min_{x\in[0,x_T]} r(x;\alpha,\beta) = \min_{x\in[0,x_T]} \sqrt{x^2 + p_{\text{rib}}(x;\alpha,\beta)}. \tag{62}$$

The minimizer of $r(x)$ over the compact interval $[0,x_T]$ is either an interior point $x_{\text{int}} \in (0,x_T)$ (circle tangent to the boundary) or the endpoint $x = x_T$ (the turning location, which in saddle-shifted coordinates $\xi = x-\pi$ equals $\xi = -\arcsin\beta$). The standard tangency condition is therefore valid only if the minimum is attained in the interior. To decide which case holds, set

$$R(x) := r(x)^2 = x^2 + p_{\text{rib}}(x). \tag{63}$$

Using that p_{rib} satisfies the branch equation (52) with $\sigma = +1$,

$$p'_{\text{rib}}(x) = -2\alpha p_{\text{rib}}(x) - 2\sin x - 2\beta, \tag{64}$$

one obtains

$$R'(x) = 2x + p'_{\text{rib}}(x) = 2x - 2\alpha p_{\text{rib}}(x) - 2\sin x - 2\beta. \tag{65}$$

A second derivative computation gives

$$R''(x) = 2 - 2\alpha p'_{\text{rib}}(x) - 2\cos x = 2 + 4\alpha^2 p_{\text{rib}}(x) + 4\alpha\sin x + 4\alpha\beta - 2\cos x. \tag{66}$$

On the relevant interval $x\in[0,x_T]\subset[0,\pi]$ one has $\sin x \ge 0$, $p_{\text{rib}}(x)\ge 0$, and $2-2\cos x \ge 0$, hence

$$R''(x) \ge 0 \quad \text{for all } x\in[0,x_T]. \tag{67}$$

Thus, $R'(x)$ is increasing on $[0,x_T]$, and $R(x)$ has at most one stationary point in $(0,x_T)$. Therefore the minimum of R on $[0,x_T]$ is either an interior stationary point (if it exists) or the endpoint x_T.

At the endpoint $x = x_T$ one has $p_{\text{rib}}(x_T) = 0$ and $\sin x_T = \sin(\pi - \delta_s) = \sin\delta_s = \beta$. Therefore

$$p'_{\text{rib}}(x_T) = -2\sin x_T - 2\beta = -4\beta, \qquad R'(x_T) = 2x_T + p'_{\text{rib}}(x_T) = 2x_T - 4\beta. \tag{68}$$

Moreover, at $x=0$,

$$R'(0) = -2\alpha p_{\text{rib}}(0) - 2\beta < 0. \tag{69}$$

Because R' is increasing, an interior stationary point exists if and only if $R'(x_T) > 0$, that is, if and only if

$$x_T > 2\beta \quad \Longleftrightarrow \quad \pi - \arcsin\beta > 2\beta. \tag{70}$$

Define $\beta_{\text{crit}} \in (0, 1)$ as the unique solution of the threshold equation

$$\pi - \arcsin(\beta_{\text{crit}}) = 2\beta_{\text{crit}}, \qquad \beta_{\text{crit}} \approx 0.9477471335. \tag{71}$$

Then, the LIM is given by the piecewise formula

$$r_{\text{loc}}(\alpha, \beta) = \begin{cases} \min_{x\in(0,x_T)} \sqrt{x^2 + p_{\text{rib}}(x)}, & 0 < \beta < \beta_{\text{crit}}, \\ \sqrt{x_T^2 + p_{\text{rib}}(x_T)} = x_T = \pi - \arcsin\beta, & \beta_{\text{crit}} \le \beta \le 1. \end{cases} \tag{72}$$

In particular, for $\beta \ge \beta_{\text{crit}}$ the closest point of the ribbon boundary to the origin is the endpoint $(x_T, 0)$, and the LIM is set purely by the sticking band width.

For $0 < \beta < \beta_{\text{crit}}$, the minimizer is an interior point $x = x_{\text{int}}(\alpha, \beta) \in (0, x_T)$, characterized by stationarity of $R(x)$, equivalently, tangency of the circle to the boundary

$$\frac{\mathrm{d}}{\mathrm{d}x}\big(x^2 + p_{\text{rib}}(x)\big) = 0 \quad \Longleftrightarrow \quad 2x + p'_{\text{rib}}(x) = 0. \tag{73}$$

Since p_{rib} satisfies the branch ODE (52) with $\sigma = +1$, one has $p'_{\text{rib}}(x) = -2\alpha p_{\text{rib}}(x) - 2\sin x - 2\beta$. Substituting into Equation (73) yields the convenient form

$$x = \alpha\, p_{\text{rib}}(x) + \sin x + \beta. \tag{74}$$

Combining Equation (74) with the explicit boundary (60) gives a single scalar tangency equation for $x_{\text{int}}(\alpha, \beta)$.

To write it explicitly, set $\delta_s = \arcsin\beta$ and denote

$$c_\beta := \cos\delta_s = \sqrt{1 - \beta^2}, \qquad x_T = \pi - \delta_s. \tag{75}$$

Using $\sin x_T = \beta$ and $\cos x_T = -c_\beta$ in $A_+(x_T)$ gives

$$A_+(x_T) = -\frac{2}{4\alpha^2 + 1}\big(c_\beta + 2\alpha\beta\big) - \frac{\beta}{\alpha}. \tag{76}$$

After substitution into Equation (74) one obtains the explicit transcendental equation

$$(4\alpha^2 + 1)\, x = \sin x + 2\alpha\cos x + \big(\beta + 2\alpha c_\beta + 8\alpha^2\beta\big)\, e^{2\alpha(x_T - x)}, \qquad x \in (0, x_T), \tag{77}$$

whose unique solution is $x_{\text{int}}(\alpha, \beta)$. Indeed, defining

$$F(x) := (4\alpha^2 + 1)\, x - \sin x - 2\alpha\cos x - \big(\beta + 2\alpha c_\beta + 8\alpha^2\beta\big)\, e^{2\alpha(x_T - x)}, \tag{78}$$

one finds

$$F'(x) = 4\alpha^2 + 1 - \cos x + 2\alpha\sin x + 2\alpha\big(\beta + 2\alpha c_\beta + 8\alpha^2\beta\big)e^{2\alpha(x_T - x)} > 0 \tag{79}$$

for all $x \in [0, x_T]$, so Equation (77) possesses exactly one root in $(0, x_T)$. Finally, the LIM follows by evaluating the exact boundary at this point:

$$r_{\text{loc}}(\alpha, \beta) = \sqrt{x_{\text{int}}(\alpha, \beta)^2 + p_{\text{rib}}(x_{\text{int}}(\alpha, \beta))}, \qquad 0 < \beta < \beta_{\text{crit}}. \tag{80}$$

As in Section 3.3, it is advantageous to use approximations only for x_{int} and then evaluate p_{rib} from the exact closed form (60), to avoid additional truncation error in the boundary curve itself.

(i) *Small-α expansion (fixed $\beta \in (0, \beta_{\text{crit}})$).* For $\alpha \to 0^+$ with fixed $\beta \in (0, \beta_{\text{crit}})$, $x_{\text{int}}(\alpha, \beta)$ admits a regular expansion

$$x_{\text{int}}(\alpha, \beta) = x_0 + \alpha x_1 + \alpha^2 x_2 + \mathcal{O}(\alpha^3), \tag{81}$$

where $x_0 \in (0, x_T)$ is the unique root of the limiting equation

$$x_0 - \sin x_0 = \beta, \tag{82}$$

and the next coefficients are

$$x_1 = \frac{2\big(\cos x_0 + c_\beta + \beta(x_T - x_0)\big)}{1 - \cos x_0}, \tag{83}$$

$$x_2 = \frac{4\beta(x_T - x_0)^2 + 16\beta - 4\beta x_1 + 8c_\beta(x_T - x_0) - 8x_0 - 4\sin x_0\, x_1 - \sin x_0\, x_1^2}{2(1 - \cos x_0)}. \tag{84}$$

In computations, one may insert $x_{\mathrm{sa}}(\alpha, \beta) := x_0 + \alpha x_1 + \alpha^2 x_2$ into Equation (60) and then into Equation (80).

(ii) *First-order Lambert W approximation*. Replacing $\sin x \approx x$ and $\cos x \approx 1$ in Equation (77) yields

$$(u - 1)e^u = \frac{\beta + 2\alpha c_\beta + 8\alpha^2\beta}{2\alpha}\, e^{2\alpha x_T}, \qquad u := 2\alpha x, \tag{85}$$

hence

$$x_{\mathrm{int}}(\alpha, \beta) \approx x_W(\alpha, \beta) := \frac{1 + W_0\Big(\frac{\beta + 2\alpha c_\beta + 8\alpha^2\beta}{2\alpha}\, e^{2\alpha x_T - 1}\Big)}{2\alpha}, \qquad \alpha > 0,\ \beta \in (0, \beta_{\mathrm{crit}}). \tag{86}$$

The associated r_{loc} approximation is obtained by inserting $x_W(\alpha, \beta)$ into the exact boundary (60) and then into Equation (80). This approximation is mainly useful for moderate and large α; for sufficiently small α, it may fall outside the physically relevant interval $x \in (0, x_T)$.

(iii) *Third-order truncation and generalized Lambert W (valid for $\beta \in (0, \beta_{\mathrm{crit}})$)*. Using $\sin x \approx x - \frac{x^3}{6}$ and $\cos x \approx 1 - \frac{x^2}{2}$ in Equation (77) and setting $u = 2\alpha x$ gives the cubic-exponential equation

$$\Big(u^3 + 12\alpha^2 u^2 + 96\alpha^4 u - 96\alpha^4\Big)e^u = 48\alpha^3\big(\beta + 2\alpha c_\beta + 8\alpha^2\beta\big)e^{2\alpha x_T}. \tag{87}$$

Let $u_1(\alpha), u_2(\alpha), u_3(\alpha)$ denote the roots of the cubic in Equation (87). Then, Equation (87) can be represented by the generalized Lambert W function (in the sense of *Mezö* and *Baricz* [53, 54]) as

$$u \approx W\Big(u_1(\alpha), u_2(\alpha), u_3(\alpha);\ 48\alpha^3\big(\beta + 2\alpha c_\beta + 8\alpha^2\beta\big)e^{2\alpha x_T}\Big), \qquad x_{\mathrm{int}}(\alpha, \beta) \approx x_{\mathrm{gW}}(\alpha, \beta) := \frac{u}{2\alpha}. \tag{88}$$

The physically relevant approximation corresponds to the smallest positive real solution $x_{\mathrm{gW}}(\alpha, \beta) \in (0, x_T)$, and r_{loc} again follows from the exact evaluation of Equation (80).

(iv) *Large-α asymptotics (fixed $\beta \in (0, \beta_{\mathrm{crit}})$)*. For $\alpha \to \infty$ and fixed $\beta \in (0, \beta_{\mathrm{crit}})$, the tangency point approaches the turning location $x_T = \pi - \arcsin\beta$. Set

$$x_{\mathrm{int}}(\alpha, \beta) = x_T - \delta(\alpha, \beta), \qquad u := 2\alpha\,\delta. \tag{89}$$

Balancing the dominant terms in Equation (77) gives $e^u \sim x_T/(2\beta)$, and a one-step refinement based on the next-order balance yields

$$u = \ln\Big(\frac{x_T}{2\beta}\Big) + \frac{1}{\alpha}\,\frac{-2\ln\big(\frac{x_T}{2\beta}\big) - \frac{c_\beta x_T}{\beta} + 2c_\beta}{4x_T} + \mathcal{O}\Big(\frac{1}{\alpha^2}\Big), \qquad \alpha \to \infty. \tag{90}$$

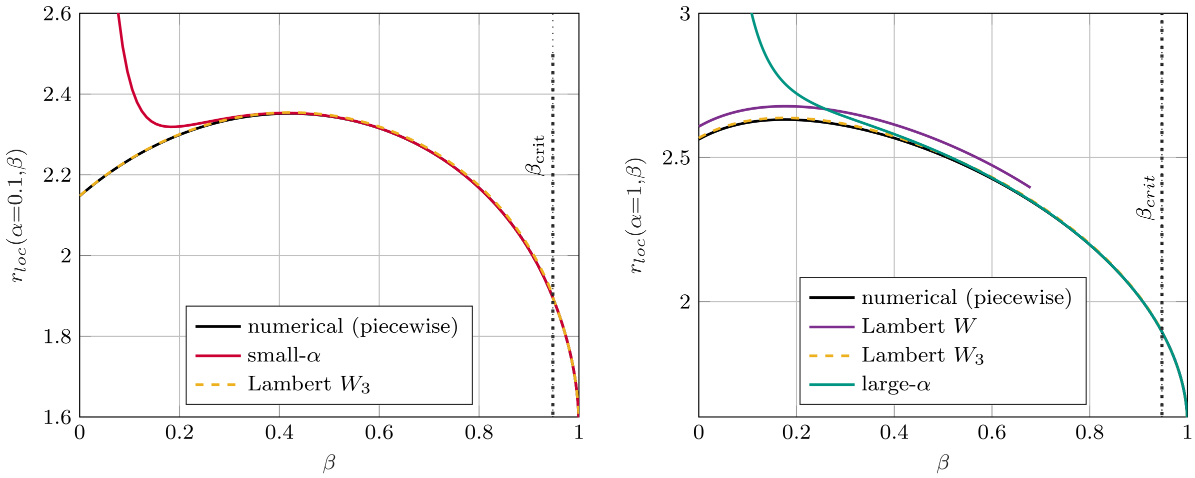

(a) β-dependency at $\alpha = 0.1$

(b) β-dependency at $\alpha = 1.0$

FIGURE 8 | LIM and its approximations for small and large α values

Since $\delta = u/(2\alpha)$, this implies

$$x_{\rm int}(\alpha,\beta) = x_T - \frac{1}{2\alpha}\ln\!\left(\frac{x_T}{2\beta}\right) - \frac{1}{2\alpha^2}\,\frac{-2\ln\!\left(\frac{x_T}{2\beta}\right) - \frac{c_\beta x_T}{\beta} + 2c_\beta}{4x_T} + \mathcal{O}\!\left(\frac{1}{\alpha^3}\right), \qquad \alpha \to \infty. \tag{91}$$

As before, the corresponding large-α approximation of $r_{\rm loc}(\alpha,\beta)$ is obtained by inserting $x_{\rm int}^{(\infty)}$ from Equation (91) into the exact boundary Equation (60) and then into Equation (80).

Endpoint regime ($\beta_{\rm crit} \le \beta \le 1$): In this case, the minimizer of $r(x)$ on $[0, x_T]$ is attained at the endpoint $x = x_T$, so the LIM reduces to

$$r_{\rm loc}(\alpha,\beta) = x_T = \pi - \arcsin\beta, \qquad \beta_{\rm crit} \le \beta \le 1, \tag{92}$$

independently of α. Equivalently, in saddle-shifted coordinates $\xi = x - \pi$ the closest boundary point is $\xi = -\arcsin\beta$ with zero velocity.

Figure 8 shows the β-dependence of the LIM for representative small and large drag values, and compares the exact evaluation of Equation (80) with the approximations obtained from (i)–(iv) via the corresponding estimates of $x_{\rm int}(\alpha,\beta)$. Figure 9 shows the α-dependence at fixed $\beta = 0.5$, indicating how the same approximations track the numerical minimizer across the drag range. A representative phase-plane geometry of the LIM construction is shown in Figure 10, where the numerical value and the small-α and generalized Lambert W estimates are compared.

5 | Cosine Potential With Normal-Force-Dependent Coulomb Friction

5.1 | Model and Regionwise Phase-Plane Representation

We consider a rigid pendulum in the periodic potential $U(x) = -\cos x$ with quadratic air drag and bearing Coulomb friction proportional to the instantaneous bearing normal force. In the standard nondimensionalization $m = l = g = 1$, the rod force is

$$T(x,\dot{x}) = \dot{x}^2 + \cos x, \tag{93}$$

so that the normal-force magnitude at the bearing is

$$N(x,\dot{x}) = |T(x,\dot{x})| = |\dot{x}^2 + \cos x|. \tag{94}$$

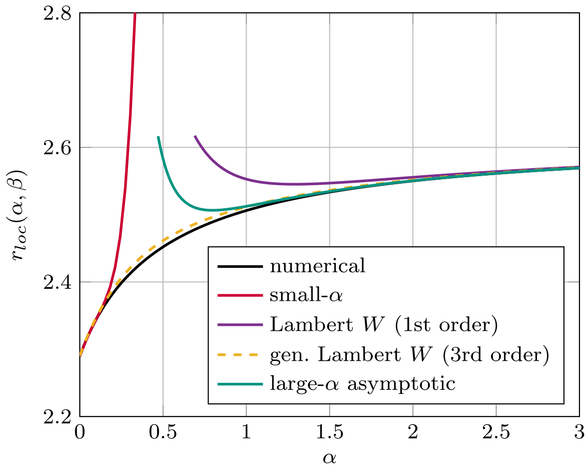

FIGURE 9 | α-dependency of the LIM and its estimates for $\beta = 0.5$.

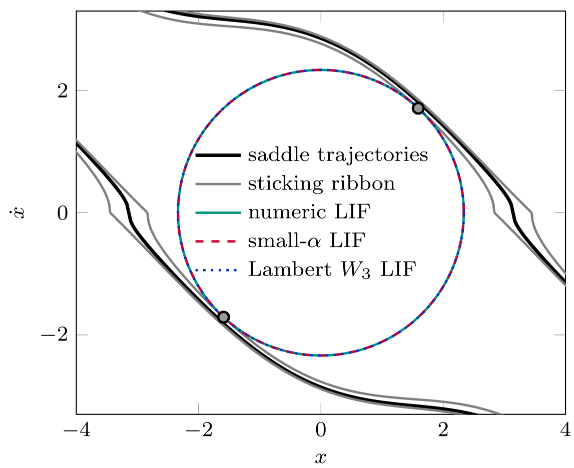

FIGURE 10 | LIM for the cosine potential with quadratic drag and Coulomb friction at $\alpha = 0.10$ and $\beta = 0.3$. Values: numerical: 2.33633, small-α: 2.34086, third-order Lambert W: 2.33798.

The generic Equation (1) assumes a Coulomb level $\beta(x)$ depending on position only. In the present problem, however, the friction torque is proportional to the instantaneous normal force and therefore depends on both x and $\dot{x}$. The effective Coulomb level becomes

$$\beta(x, \dot{x}) = \mu\,|\dot{x}^2 + \cos x|,$$

which cannot be written as a function of x alone. Hence, this example constitutes an extension of Equation (1) in which β depends on the phase variables $(x, \dot{x})$ (equivalently (x, p) with $p = \dot{x}^2$). As shown below, the branchwise reduction method still applies after a suitable partition of the phase plane.

With quadratic air drag $-\alpha|\dot{x}|\dot{x}$ ($\alpha > 0$) and Coulomb torque $-\mu N(x, \dot{x})\,\mathrm{sgn}(\dot{x})$ ($\mu \geq 0$), the equation of motion reads

$$\ddot{x} + \alpha|\dot{x}|\,\dot{x} + \mu\,|\dot{x}^2 + \cos x|\;\mathrm{sgn}(\dot{x}) + \sin x = 0, \qquad \alpha > 0,\ \mu \geq 0. \tag{95}$$

On any trajectory segment with fixed velocity sign $\sigma = \mathrm{sgn}(\dot{x}) \in \{+1, -1\}$, introduce the squared velocity $p(x) = \dot{x}^2$. Then, away from rest ($\dot{x} \neq 0$),

$$\frac{\mathrm{d}p}{\mathrm{d}x} = 2\ddot{x} = -2\sin x - 2\alpha\sigma\,p - 2\mu\sigma\,|p + \cos x|. \tag{96}$$

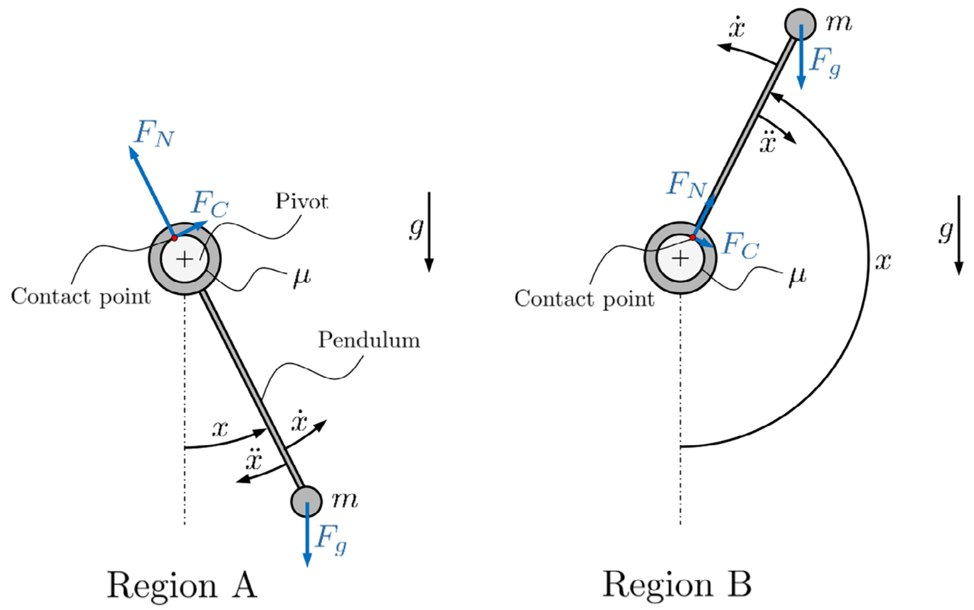

FIGURE 11 | Rigid pendulum of length l and bob mass m in a gravitational field. The angular coordinate x is measured from the downward vertical. At the bearing, Coulomb friction is characterized by the coefficient μ, while the normal load depends on the instantaneous rod force.

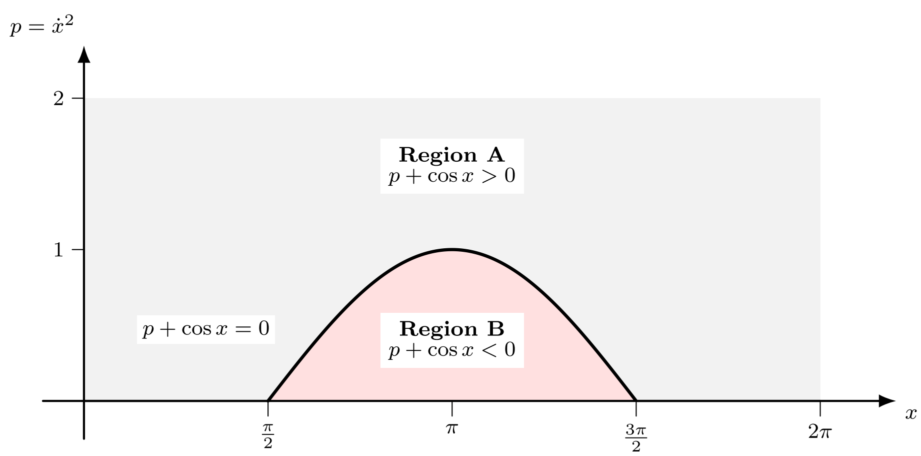

FIGURE 12 | Schematic partition of the (x, p) plane with $p = \dot{x}^2$ by the switching curve $p + \cos x = 0$. Region A corresponds to $p + \cos x \geq 0$ and Region B to $p + \cos x \leq 0$.

The absolute value $|p + \cos x|$ reflects the switching of the loaded bearing side. It is convenient to split the phase plane into the two regions

$$\text{Region A:} \quad p + \cos x > 0, \tag{97}$$

$$\text{Region B:} \quad p + \cos x < 0. \tag{98}$$

For a graphical representation of the two regions, see Figure 11. The partitioning in the x–p plane is depicted in Figure 12. In each region, Equation (96) becomes linear.

Region A ($p + \cos x \geq 0$) Here $|p + \cos x| = p + \cos x$, hence

$$\frac{\mathrm{d}p}{\mathrm{d}x} + 2(\alpha + \mu)\sigma\, p = -2 \sin x - 2\mu\sigma \cos x. \tag{99}$$

With integrating factor $e^{2(\alpha+\mu)\sigma x}$, the branch through (x_0, v_0), admits the closed form

$$p_{A,\sigma}(x; x_0, v_0) = A_{A,\sigma}(x) + e^{-2(\alpha+\mu)\sigma(x-x_0)}\left[v_0^2 - A_{A,\sigma}(x_0)\right], \tag{100}$$

where

$$A_{A,\sigma}(x) := \frac{2}{4(\alpha+\mu)^2+1}(\cos x - 2(\alpha+\mu)\sigma \sin x) - \frac{2\mu\sigma}{4(\alpha+\mu)^2+1}(\sin x + 2(\alpha+\mu)\sigma\cos x). \tag{101}$$

Equation (100) is valid as long as $p_{A,\sigma}(x) + \cos x \geq 0$.

Region B ($p + \cos x \leq 0$) Here $|p + \cos x| = -(p + \cos x)$, hence

$$\frac{\mathrm{d}p}{\mathrm{d}x} + 2(\alpha-\mu)\sigma\, p = -2\sin x + 2\mu\sigma\cos x. \tag{102}$$

Analogously,

$$p_{B,\sigma}(x; x_0, v_0) = A_{B,\sigma}(x) + e^{-2(\alpha-\mu)\sigma(x-x_0)}\left[v_0^2 - A_{B,\sigma}(x_0)\right], \tag{103}$$

where

$$A_{B,\sigma}(x) := \frac{2}{4(\alpha-\mu)^2+1}(\cos x - 2(\alpha-\mu)\sigma \sin x) + \frac{2\mu\sigma}{4(\alpha-\mu)^2+1}(\sin x + 2(\alpha-\mu)\sigma\cos x). \tag{104}$$

Equation (103) is valid as long as $p_{B,\sigma}(x) + \cos x \leq 0$. For later use, we set $k_A := \alpha + \mu$ and $k_B := \alpha - \mu$. On any interval where $p(x) \geq 0$, the velocity is $\dot{x} = \sigma\sqrt{p(x)}$. Turning points satisfy $p = 0$ and trigger a branch switch $\sigma \mapsto -\sigma$. Crossings of the curve $p + \cos x = 0$ trigger a region switch between Equation (100) and Equation (103) with continuous matching of p.

5.2 | Basins of Attraction, Rotations, and Sticking Ribbons

The saddles remain at $x_{s,n} = (2n+1)\pi$. For right-going initial motion ($v_0 > 0$) starting in the reference cell $x_0 \in (-\pi, \pi)$, the critical condition for reaching the saddle $x_{s,n}$ with zero velocity is again

$$p(x_{s,n}; x_0, v_0) = 0, \tag{105}$$

but now $p(\cdot)$ is constructed by concatenating Region-A and Region-B pieces, with matching across $p + \cos x = 0$ if such a crossing occurs along the path to $x_{s,n}$. The resulting critical curves $v^2_{\mathrm{crit},n}(x_0; \alpha, \mu)$ still form ordered stripes and determine the rotation count via

$$N = \#\left\{n \geq 0 :\ v_0^2 \geq v^2_{\mathrm{crit},n}(x_0; \alpha, \mu)\right\}. \tag{106}$$

There is also a sticking interval in this case. At $\dot{x} = 0$, one has $N(x, 0) = |\cos x|$. A static equilibrium is admissible whenever the restoring torque can be balanced by a friction torque of magnitude at most $\mu|\cos x|$, that is,

$$|\sin x| \leq \mu|\cos x| \quad \Longleftrightarrow \quad |\tan x| \leq \mu. \tag{107}$$

Around the saddle $x_s = \pi$, this defines the sticking interval

$$x_{s,-} \leq x \leq x_{s,+}, \qquad x_{s,\pm} := \pi \pm \delta_s, \qquad \delta_s := \arctan\mu, \qquad \mu \geq 0. \tag{108}$$

As before, the phase portrait contains ribbon-shaped sets of initial conditions whose first turning point falls inside $[x_{s,-}, x_{s,+}]$, after which the motion terminates in a stuck state near the top. For the upper-right quadrant ($x \geq 0, \dot{x} \geq 0$), the relevant ribbon boundary, closer to the origin, is obtained by requiring that the first turning point equals the left endpoint

$$x_T := x_{s,-} = \pi - \delta_s = \pi - \arctan\mu. \tag{109}$$

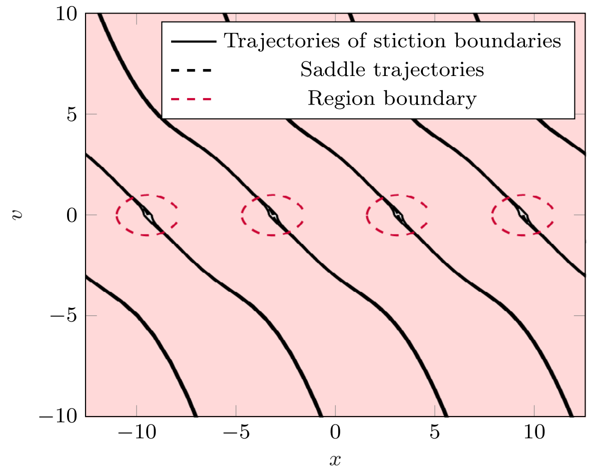

FIGURE 13 | Sticking ribbons for $\alpha = 0.03$ and $\mu = 0.3$.

We define $p_{\text{rib}}(x; \alpha, \mu)$ as the unique nonnegative solution of Equation (96) on $x \in [0, x_T]$ satisfying the turning condition

$$p_{\text{rib}}(x_T; \alpha, \mu) = 0, \qquad \dot{x} = +\sqrt{p_{\text{rib}}(x; \alpha, \mu)}. \tag{110}$$

Since $\cos x_T < 0$, the turning point lies in Region B. Hence, near x_T the boundary is given by the Region-B formula with $\sigma = +1$ and initial condition $(x_0, p_0) = (x_T, 0)$:

$$p_B^{(T)}(x; \alpha, \mu) := A_{B,+}(x) - e^{2(\alpha-\mu)(x_T - x)} A_{B,+}(x_T), \qquad x \le x_T, \tag{111}$$

where $A_{B,+}$ is given by Equation (104) with $\sigma = +1$.

Let $x_c = x_c(\alpha, \mu) \in (0, x_T)$ denote the unique crossing point where the boundary meets the region-separating curve $p + \cos x = 0$, defined by

$$p_B^{(T)}(x_c; \alpha, \mu) + \cos x_c = 0. \tag{112}$$

On $[x_c, x_T]$ one has $p_{\text{rib}} = p_B^{(T)}$ (Region B). For $x < x_c$, the boundary continues in Region A, obtained by matching at (x_c, p_c) with $p_c = p_{\text{rib}}(x_c) = -\cos x_c$, and using the Region-A explicit solution:

$$p_A^{(T)}(x; \alpha, \mu) := A_{A,+}(x) + e^{-2(\alpha+\mu)(x - x_c)} \left[(-\cos x_c) - A_{A,+}(x_c) \right], \qquad 0 \le x \le x_c, \tag{113}$$

with $A_{A,+}$ from Equation (101) at $\sigma = +1$. In summary,

$$p_{\text{rib}}(x; \alpha, \mu) = \begin{cases} p_A^{(T)}(x; \alpha, \mu), & x \le x_c(\alpha, \mu), \\ p_B^{(T)}(x; \alpha, \mu), & x_c(\alpha, \mu) \le x \le x_T. \end{cases} \tag{114}$$

Figures 13 and 14 illustrate the resulting sticking ribbons. Unfortunately, the concatenation condition at the region boundary, that is, the implicit equation defining the switch point x_c via Equation (112) (and the associated matching of the pieces), does not admit a closed-form analytic solution in general. Therefore, we proceed to a numerical analysis in the following.

5.3 | LIM Determined by the Sticking-Ribbon Boundary

We define the LIM with respect to the *attracting regime* in the lower part of the potential, using (0,0) as its center. Specifically, $r_{\text{loc}}(\alpha, \mu)$ is the largest radius such that the closed disk $x^2 + \dot{x}^2 \le r_{\text{loc}}^2$ lies entirely inside the set of initial conditions whose trajectories eventually come to rest within this lower-well attracting regime (not necessarily at (0,0)). Equivalently, $r_{\text{loc}}(\alpha, \mu)$ is the minimum Euclidean distance from the origin to the boundary of this attracting set. For $\mu > 0$,

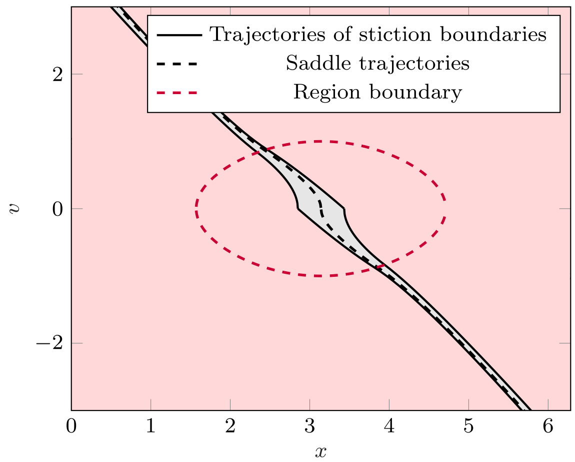

FIGURE 14 | Sticking ribbons for $\alpha = 0.05$ and $\mu = 0.3$.

the closest obstruction is sticking near the neighboring saddle at $x = \pi$, hence the LIM is determined by the distance to the upper-right sticking-ribbon boundary $p_{\text{rib}}(x; \alpha, \mu)$ from Equation (114). We define along the boundary

$$r(x; \alpha, \mu) := \sqrt{x^2 + p_{\text{rib}}(x; \alpha, \mu)}, \qquad x \in [0, x_T], \tag{115}$$

so that

$$r_{\text{loc}}(\alpha, \mu) = \min_{x \in [0, x_T]} r(x; \alpha, \mu) = \min_{x \in [0, x_T]} \sqrt{x^2 + p_{\text{rib}}(x; \alpha, \mu)}. \tag{116}$$

The relevant turning endpoint is $x_T(\mu)$ from Equation (109), hence it is independent of α. The ribbon boundary pieces $p_B^{(T)}$, the region-switch point x_c, the matched continuation $p_A^{(T)}$, and so, the piecewise graph p_{rib} are already defined by Equations (111)–(114), respectively.

Because p_{rib} is continuous and piecewise smooth, the minimizer of $r(x)$ over $[0, x_T]$ is among:

- a stationary point in Region A, solving $R'(x) = 0$ on $(0, x_c)$,
- at the boundary region x_c solving $R'(x) = 0$,
- a stationary point in Region B, solving $R'(x) = 0$ on (x_c, x_T),
- the endpoint $x = x_T$.

Here

$$R(x) := r(x)^2 = x^2 + p_{\text{rib}}(x), \qquad R'(x) = 2x + p'_{\text{rib}}(x). \tag{117}$$

On Region A, p_{rib} satisfies Equation (99) with $\sigma = +1$, hence

$$p'_{\text{rib}}(x) = -2\sin x - 2\mu\cos x - 2(\alpha + \mu)p_{\text{rib}}(x) = -2\sin x - 2\mu\cos x - 2k_A\, p_{\text{rib}}(x), \tag{118}$$

and $R'(x) = 0$ becomes

$$x = k_A\, p_{\text{rib}}(x; \alpha, \mu) + \sin x + \mu\cos x, \qquad x \in (0, x_c). \tag{119}$$

On Region B, p_{rib} satisfies Equation (102) with $\sigma = +1$, hence

$$p'_{\text{rib}}(x) = -2\sin x + 2\mu\cos x - 2(\alpha - \mu)p_{\text{rib}}(x) = -2\sin x + 2\mu\cos x - 2k_B\, p_{\text{rib}}(x), \tag{120}$$

and $R'(x) = 0$ becomes

$$x = k_B\, p_{\text{rib}}(x; \alpha, \mu) + \sin x - \mu\cos x, \qquad x \in (x_c, x_T). \tag{121}$$

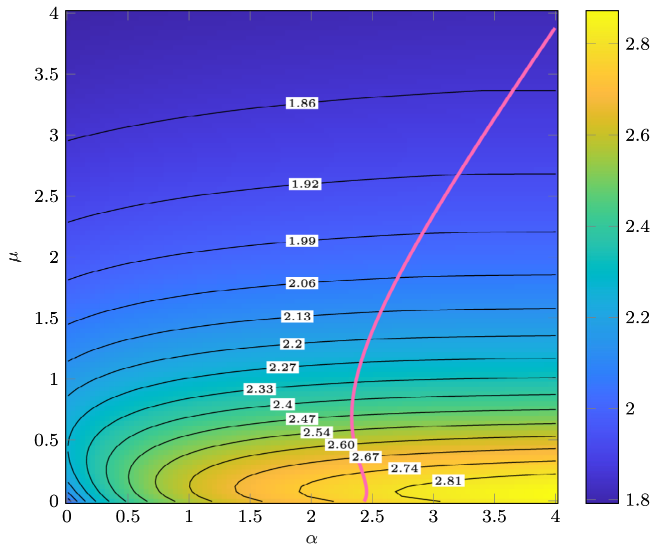

FIGURE 15 | LIM (given by the color scale) depending on α and μ. The pink line shows the region boundary regarding the tangency point of the LIM circle and the ribbon boundary. On the left of the line, tangency occurs in Region A; on the right of the line, it occurs in Region B.

Once a candidate x_* is found numerically, the LIM value follows from

$$r_{\text{loc}}(\alpha, \mu) = \sqrt{x_*^2 + p_{\text{rib}}(x_*; \alpha, \mu)}. \tag{122}$$

Comparing all (existing) candidate values, the LIM is determined. In Figure 15, the numerically found values of the LIM are depicted depending on the values of α and μ. Interestingly, the function is monotonically increasing in α; however, in μ, it first increases, then decreases. It is also interesting to note in which regime the minimizer x_* is located. In Figure 15, the region located to the left of the pink line corresponds to tangency of the LIM circle to the sticking ribbon in Region A, and only for sufficiently large α it moves to Region B, located to the right of the pink curve. The pink curve corresponds to the case where the tangency point lies exactly on the boundary of the region defined by $p + \cos(x) = 0$.

6 | Washboard Potential

6.1 | Model, Equilibria, Branchwise Reduction, and Closed-Form Phase Trajectories

We now replace the cosine potential with the tilted periodic (washboard) potential

$$U_F(x) = -\cos x - Fx, \qquad F \in \mathbb{R}, \tag{123}$$

which is the standard way to include a constant bias (force or torque) in an otherwise periodic potential (see Figure 16). Closely related reduced pendulum-type models arise in the context of capture into resonance, while driven pendulum models also play a central role in autoresonance [55–58]. A direct example is a pendulum subject to a constant external torque (e.g., a motor torque or a constant load torque), where F is proportional to the applied torque. Differentiating Equation (123) yields

$$U_F'(x) = \sin x - F, \tag{124}$$

so that with quadratic air drag, the autonomous equation of motion becomes

$$\ddot{x} + \alpha|\dot{x}|\,\dot{x} + \sin x - F = 0, \qquad \alpha > 0. \tag{125}$$

Introduce the velocity sign $\sigma = \operatorname{sgn}(\dot{x}) \in \{+1, -1\}$. On any sliding branch with fixed σ, we have $|\dot{x}|\,\dot{x} = \sigma\dot{x}^2$ and therefore

$$\ddot{x} = F - \sin x - \alpha\sigma\,\dot{x}^2. \tag{126}$$

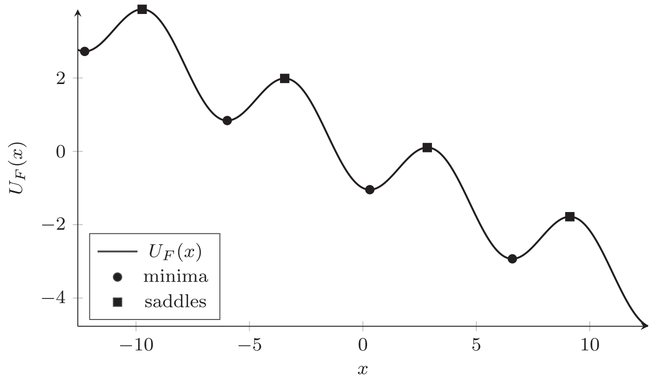

FIGURE 16 | Tilted periodic (washboard) potential $U_F(x) = -\cos x - Fx$ for a representative tilt $F = 0.3$. For $|F| < 1$, the potential retains local minima $x_{m,k} = \delta + 2k\pi$ and saddles $x_{s,k} = \pi - \delta + 2k\pi$, where $\delta = \arcsin F$.

For $|F| < 1$, the washboard retains equilibria (local wells) given by $\sin x = F$. Writing

$$\delta := \arcsin F \in \left(-\frac{\pi}{2}, \frac{\pi}{2}\right), \tag{127}$$

the stable minima and unstable saddles are

$$x_{m,k} = \delta + 2k\pi, \qquad x_{s,k} = \pi - \delta + 2k\pi, \qquad k \in \mathbb{Z}, \tag{128}$$

with $\cos x_{m,k} = \sqrt{1-F^2} > 0$ and $\cos x_{s,k} = -\sqrt{1-F^2} < 0$. For $|F| \geq 1$, the potential is monotone, and no equilibria exist; in that regime, the outcomes are transport-type only.

As before, on any branch where $\dot{x} \neq 0$ we introduce

$$p(x) := \dot{x}^2 \geq 0. \tag{129}$$

Using $\mathrm{d}p/\mathrm{d}x = 2\ddot{x}$ and Equation (126), the squared-velocity equation on a fixed-σ branch becomes

$$\frac{\mathrm{d}p}{\mathrm{d}x} + 2\alpha\sigma\, p = 2\big(F - \sin x\big), \qquad p(x) = \dot{x}^2. \tag{130}$$

Turning points satisfy $p = 0$ and require switching to the opposite sign branch $-\sigma$. We now solve Equation (130) explicitly to obtain closed-form phase trajectories on each fixed-σ branch. Equation (130) is linear and differs from the untilted cosine case only by the constant forcing term $2F$. For initial data (x_0, v_0) with $v_0 \neq 0$ and $\sigma = \mathrm{sgn}(v_0)$, solving Equation (130) gives

$$p_\sigma(x; x_0, v_0) = A_\sigma^{(F)}(x) + e^{-2\alpha\sigma(x-x_0)}\left[v_0^2 - A_\sigma^{(F)}(x_0)\right], \tag{131}$$

where the particular solution is

$$A_\sigma^{(F)}(x) := \frac{2}{4\alpha^2+1}(\cos x - 2\alpha\sigma \sin x) + \frac{F}{\alpha\sigma}. \tag{132}$$

On any interval where $p_\sigma(x) \geq 0$ the velocity is $\dot{x} = \sigma\sqrt{p_\sigma(x)}$.

6.2 | Trapping Versus Escape: Critical Damping

A qualitative novelty of the washboard is the possibility of indefinite transport even in the autonomous setting, because $U_F(x) \to -\infty$ as $x \to +\infty$ for $F > 0$. Fix $|F| < 1$ and consider right-going motion ($\sigma = +1$), so that $\dot{x} > 0$ and the quadratic drag reads $\alpha\dot{x}^2$. From Equation (131) the transient term $e^{-2\alpha(x-x_0)}\left[v_0^2 - A_+^{(F)}(x_0)\right]$ decays as $x \to +\infty$, hence the long-x behavior is governed by the particular function $A_+^{(F)}(x)$.

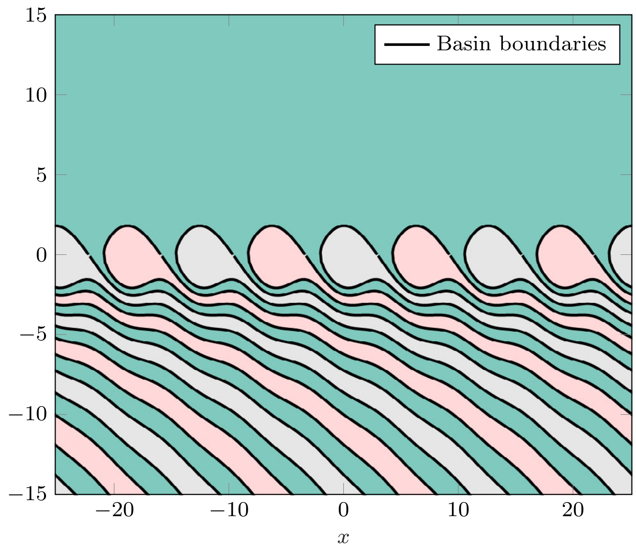

FIGURE 17 | Verification of the analytically found basin-of-attraction boundary against numerical simulation data for $\alpha = 0.05$ and $F = 0.2$. Gray and rose domains depict safe basins, while the green regions correspond to initial conditions with escaping trajectories.

If $A_+^{(F)}(x) > 0$ for all x, then $p(x) \to A_+^{(F)}(x)$ and a right-going running attractor exists with asymptotically periodic velocity profile $\dot{x}(x) = \sqrt{A_+^{(F)}(x)}$. Trajectories in its basin cross infinitely many barriers (an infinite number of rotations), which is the mechanism behind the green escape set in Figure 17. Conversely, if $A_+^{(F)}$ attains a nonpositive value, then the decaying transient cannot prevent p from reaching 0 on the right-going branch, so a turning point occurs and capture into a local well becomes possible. Thus, a sharp criterion for the existence of running motion is

$$\min_{x \in \mathbb{R}} A_+^{(F)}(x) > 0. \tag{133}$$

To evaluate the minimum, write

$$A_+^{(F)}(x) = \frac{F}{\alpha} + \frac{2}{4\alpha^2 + 1}(\cos x - 2\alpha \sin x), \tag{134}$$

whose oscillatory part has amplitude

$$\frac{2}{4\alpha^2 + 1}\sqrt{1 + 4\alpha^2} = \frac{2}{\sqrt{4\alpha^2 + 1}}. \tag{135}$$

Hence

$$\min_x A_+^{(F)}(x) = \frac{F}{\alpha} - \frac{2}{\sqrt{4\alpha^2 + 1}}. \tag{136}$$

Condition (133) is therefore equivalent to

$$\frac{F}{\alpha} > \frac{2}{\sqrt{4\alpha^2 + 1}}. \tag{137}$$

For $0 < F < 1$, the boundary case defines an explicit critical damping level

$$\alpha_{\mathrm{crit}}(F) := \frac{F}{2\sqrt{1 - F^2}}, \qquad 0 < F < 1. \tag{138}$$

A graphical representation of Equation (138) is given in Figure 18. The result agrees with Figure 17 for $\alpha = 0.05$ and $F = 0.2$, since for this F value $\alpha_{\mathrm{crit}}(0.2) \approx 0.102$, thus escaping solutions exist.

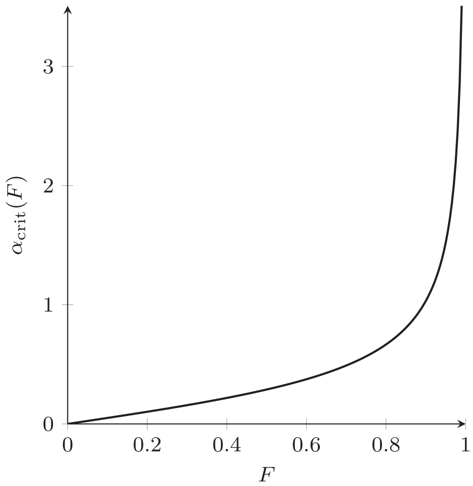

FIGURE 18 | Critical damping $\alpha_{\text{crit}}(F) = \dfrac{F}{2\sqrt{1-F^2}}$ as a function of F.

It is also useful to identify where the minimum of $A_+^{(F)}$ is attained. Since

$$\cos x - 2\alpha \sin x = \sqrt{1+4\alpha^2}\,\cos\bigl(x + \arctan(2\alpha)\bigr), \tag{139}$$

the minimum of $A_+^{(F)}$ occurs at

$$x_{\min} = \pi - \arctan(2\alpha) + 2k\pi, \qquad k \in \mathbb{Z}, \tag{140}$$

and Equation (136) follows immediately.

The value of $A_+^{(F)}$ at the saddle is nevertheless of special interest. Using $\sin x_{s,0} = F$ and $\cos x_{s,0} = -\sqrt{1-F^2}$, one finds

$$A_+^{(F)}(x_{s,0}) = \frac{F - 2\alpha\sqrt{1-F^2}}{\alpha(4\alpha^2+1)}. \tag{141}$$

Hence, $A_+^{(F)}(x_{s,0}) > 0$ is equivalent to $\alpha < \alpha_{\text{crit}}(F)$.

Finally, the curves obtained from the condition

$$p(x_{s,n}) = 0, \qquad x_{s,n} = \pi - \delta + 2n\pi, \tag{142}$$

describe stable-manifold type basin boundaries associated with pinned outcomes (capture in a well after finitely many crossings). When $\alpha < \alpha_{\text{crit}}(F)$, these boundaries coexist with a running basin leading to infinite barrier crossings; they do not preclude it.

For $F < 0$, the same transport criterion holds after left–right symmetry, with running motion occurring to the left on the $\sigma = -1$ branch. It is therefore convenient to write the threshold in the symmetric form

$$\alpha_{\text{crit}}^{\pm}(F) := \frac{|F|}{2\sqrt{1-F^2}}, \qquad 0 < |F| < 1, \tag{143}$$

where right-going transport corresponds to $F > 0$ and left-going transport to $F < 0$. For $|F| \geq 1$, there are no wells and the motion is necessarily transport-type.

6.3 | LIM of the Stable Equilibrium in the Tilted Well

In this section, we assume $0 \leq F < 1$, so that the downhill direction is to the right and the relevant neighboring saddle is $x_{s,0} = \pi - \delta$. The attractor in the reference well is the stable equilibrium $x_{m,0} = \delta$ with $\delta = \arcsin F$. The LIM is defined as the largest radius $r_{\text{loc}}(\alpha, F)$ for which the closed disk centered at the equilibrium,

$$(x-\delta)^2 + \dot{x}^2 \le r_{\text{loc}}^2, \tag{144}$$

is entirely contained in the basin of attraction of $(\delta, 0)$. Equivalently, $r_{\text{loc}}(\alpha, F)$ is the minimum Euclidean distance from $(\delta, 0)$ to the basin boundary.

The relevant basin-boundary segment is the saddle separatrix on the right-going branch ($\sigma = +1$) that approaches the neighboring saddle $x_{s,0} = \pi - \delta$ from the left. For $-1 < F < 0$, the completely symmetric construction uses the left-going branch $\sigma = -1$ and the neighboring saddle $x_{s,-1} = -\pi - \delta$; equivalently, one may obtain the corresponding formulas by the transformation

$$x \mapsto -x, \qquad F \mapsto -F. \tag{145}$$

The separatrix is characterized by the saddle condition $p(x_{s,0}) = 0$ and follows from Equation (131) with $(x_0, v_0) = (x_{s,0}, 0)$:

$$p_+(x; x_{s,0}) = A_+^{(F)}(x) - e^{2\alpha(x_{s,0} - x)} A_+^{(F)}(x_{s,0}), \qquad x \le x_{s,0}. \tag{146}$$

On the portion where $p_+ \ge 0$ the basin boundary is

$$\dot{x} = +\sqrt{p_+(x; x_{s,0})}. \tag{147}$$

If $\alpha < \alpha_{\text{crit}}(F)$, then $A_+^{(F)}(x_{s,0}) > 0$ and $p_+(x; x_{s,0})$ admits a second root $x_T < x_{m,0} = \delta$ (a turning point) in addition to $x_{s,0}$. If $\alpha \ge \alpha_{\text{crit}}(F)$, then $A_+^{(F)}(x_{s,0}) \le 0$ and no turning point exists, so the $\sigma = +1$ branch stays strictly positive for all $x < x_{s,0}$. To measure distance from $(\delta, 0)$ we shift by the equilibrium and introduce

$$R(x) := (x-\delta)^2 + p_+(x; x_{s,0}), \qquad r(x) := \sqrt{R(x)}. \tag{148}$$

Accordingly, the LIM is given by

$$r_{\text{loc}}(\alpha, F) = \begin{cases} \min\limits_{x \in [x_T, x_{s,0}]} \sqrt{(x-\delta)^2 + p_+(x; x_{s,0})}, & \alpha < \alpha_{\text{crit}}(F), \\ \inf\limits_{x \le x_{s,0}} \sqrt{(x-\delta)^2 + p_+(x; x_{s,0})}, & \alpha \ge \alpha_{\text{crit}}(F). \end{cases} \tag{149}$$

Lemma 1 (Turning point cannot be a minimizer). *Assume $\alpha < \alpha_{\text{crit}}(F)$ so that the turning point x_T exists and satisfies $p_+(x_T; x_{s,0}) = 0$. Then, R is strictly decreasing at x_T. In particular,*

$$\min_{x \in [x_T, x_{s,0}]} R(x) < R(x_T) = (x_T - \delta)^2, \tag{150}$$

and therefore the minimizer defining the LIM cannot occur at the turning point.

Proof. On the $\sigma = +1$ branch, the phase-plane equation reads

$$p_+'(x; x_{s,0}) + 2\alpha\, p_+(x; x_{s,0}) = 2(F - \sin x). \tag{151}$$

Since $p_+(x_T; x_{s,0}) = 0$, evaluating at $x = x_T$ gives

$$p_+'(x_T; x_{s,0}) = 2(F - \sin x_T). \tag{152}$$

Consequently,

$$R'(x_T) = 2(x_T - \delta) + p_+'(x_T; x_{s,0}) = 2(x_T - \delta) + 2(F - \sin x_T). \tag{153}$$

Using $F = \sin\delta$ and applying the mean value theorem to $\sin(\cdot)$ on the interval (x_T, δ), there exists $\xi \in (x_T, \delta)$ such that

$$F - \sin x_T = \sin\delta - \sin x_T = \cos\xi\,(\delta - x_T). \tag{154}$$

Therefore,

$$\frac{1}{2}R'(x_T) = (x_T - \delta) + (F - \sin x_T) = -(\delta - x_T) + \cos\xi\,(\delta - x_T) = -(1-\cos\xi)(\delta - x_T) < 0, \tag{155}$$

because $\delta - x_T > 0$ and $\cos\xi < 1$. Hence, R is strictly decreasing at x_T, which proves the claim. □

It remains to exclude the other endpoint possibilities. At the saddle endpoint $x = x_{s,0}$, one has $p_+(x_{s,0}; x_{s,0}) = 0$ and $\sin x_{s,0} = F$, hence

$$R'(x_{s,0}) = 2(x_{s,0} - \delta) + p'_+(x_{s,0}; x_{s,0}) \tag{156}$$

$$= 2(x_{s,0} - \delta) + 2(F - \sin x_{s,0}) \tag{157}$$

$$= 2(\pi - 2\delta) > 0. \tag{158}$$

Therefore, $x_{s,0}$ cannot be a minimizer of R. If $\alpha < \alpha_{\text{crit}}(F)$, the only remaining endpoint is the turning point x_T, and the lemma excludes it. If $\alpha \geq \alpha_{\text{crit}}(F)$, then there is no turning point and the admissible branch extends to $x \to -\infty$. In that case, $R(x) \to \infty$ as $x \to -\infty$, since either the exponential term in $p_+(x; x_{s,0})$ is unbounded or, in the borderline case $A_+^{(F)}(x_{s,0}) = 0$, one still has $(x-\delta)^2 \to \infty$. Hence, the minimum cannot occur at infinity.
Consequently, the LIM is attained at an interior tangency point $x = x_{\text{int}}(\alpha, F)$ satisfying stationarity of R:

$$\frac{d}{dx}\big((x-\delta)^2 + p_+(x; x_{s,0})\big) = 0 \quad \Longleftrightarrow \quad 2(x-\delta) + p'_+(x; x_{s,0}) = 0. \tag{159}$$

Using again $p'_+(x; x_{s,0}) + 2\alpha\, p_+(x; x_{s,0}) = 2(F - \sin x)$, Equation (159) becomes the tangency relation

$$x - \delta = \alpha\, p_+(x; x_{s,0}) + \sin x - F. \tag{160}$$

Substituting Equation (146) into Equation (160) and using $(4\alpha^2+1)\alpha A_+^{(F)}(x_{s,0}) = F - 2\alpha\sqrt{1-F^2}$ yields the transcendental equation for $x_{\text{int}}(\alpha, F)$:

$$(4\alpha^2+1)(x-\delta) = \sin x + 2\alpha\cos x - \big(F - 2\alpha\sqrt{1-F^2}\big)e^{2\alpha(x_{s,0}-x)}. \tag{161}$$

Finally,

$$r_{\text{loc}}(\alpha, F) = \sqrt{(x_{\text{int}} - \delta)^2 + p_+\big(x_{\text{int}}; x_{s,0}\big)}, \tag{162}$$

with p_+ given by Equation (146).
Closed-form solutions are not available for x_{int}. We therefore approximate Equation (161) by a third-order truncation about $x = \delta$, followed by the generalized Lambert W construction of *Mező* and *Baricz* [53, 54].
We set $x = \delta + y$, $u := 2\alpha y$, and $c := \sqrt{1-F^2}$. Using the third-order expansions of $\sin(\delta + y)$ and $\cos(\delta + y)$ in Equation (161), one obtains

$$\big((2\alpha F - c)\,u^3 - 6\alpha\big(F + 2\alpha c\big)\,u^2 + 24\alpha^2\big(c - 2\alpha F - 4\alpha^2 - 1\big)\,u + 48\alpha^3\big(F + 2\alpha c\big)\big)e^u = 48\alpha^3\big(F - 2\alpha c\big)e^{2\alpha(\pi - 2\delta)}. \tag{163}$$

If $2\alpha F \neq c$, division by $2\alpha F - c$ yields

$$\big(u^3 + a_2(\alpha, F)\,u^2 + a_1(\alpha, F)\,u + a_0(\alpha, F)\big)e^u = K_{\text{int}}(\alpha, F), \tag{164}$$

where

$$a_2(\alpha, F) = -\frac{6\alpha\big(F + 2\alpha c\big)}{2\alpha F - c}, \tag{165}$$

$$a_1(\alpha, F) = \frac{24\alpha^2\left(c - 2\alpha F - 4\alpha^2 - 1\right)}{2\alpha F - c}, \tag{166}$$

$$a_0(\alpha, F) = \frac{48\alpha^3\left(F + 2\alpha c\right)}{2\alpha F - c}, \tag{167}$$

$$K_{\text{int}}(\alpha, F) = \frac{48\alpha^3\left(F - 2\alpha c\right)}{2\alpha F - c}\, e^{2\alpha(\pi - 2\delta)}. \tag{168}$$

Let u_1, u_2, u_3 denote the roots of $u^3 + a_2u^2 + a_1u + a_0 = 0$. Then, Equation (164) has the canonical form $e^u \prod_{j=1}^{3}(u - u_j) = K_{\text{int}}$, hence

$$u_{\text{int}} \approx W(u_1, u_2, u_3;\, K_{\text{int}}(\alpha, F)), \qquad x_{\text{int}} \approx \delta + \frac{u_{\text{int}}}{2\alpha}, \tag{169}$$

where the relevant approximation corresponds to the smallest positive real solution.

The normalization above is singular on the exceptional curve

$$2\alpha F = c = \sqrt{1 - F^2}, \tag{170}$$

which, for $0 \le F < 1$, is equivalently parameterized by

$$F = F_{\text{exc}}(\alpha) := \frac{1}{\sqrt{1 + 4\alpha^2}}, \qquad c = c_{\text{exc}}(\alpha) := \frac{2\alpha}{\sqrt{1 + 4\alpha^2}}, \tag{171}$$

$$\delta = \delta_{\text{exc}}(\alpha) := \arcsin\left(\frac{1}{\sqrt{1 + 4\alpha^2}}\right) = \arctan\left(\frac{1}{2\alpha}\right). \tag{172}$$

On this curve, the cubic coefficient in Equation (163) vanishes, and the third-order reduction degenerates to the one-parameter quadratic-exponential equation

$$\left(u^2 + 4\alpha\sqrt{1 + 4\alpha^2}\, u - 8\alpha^2\right)e^u = K_{\text{int}}^{(2)}(\alpha), \tag{173}$$

where

$$K_{\text{int}}^{(2)}(\alpha) = -\frac{8\alpha^2(1 - 4\alpha^2)}{1 + 4\alpha^2}\, \exp(2\alpha(\pi - 2\delta_{\text{exc}}(\alpha))). \tag{174}$$

Let $u_+(\alpha)$ and $u_-(\alpha)$ denote the roots of

$$u^2 + 4\alpha\sqrt{1 + 4\alpha^2}\, u - 8\alpha^2 = 0, \tag{175}$$

namely

$$u_\pm(\alpha) = -2\alpha\sqrt{1 + 4\alpha^2} \pm 2\alpha\sqrt{3 + 4\alpha^2}. \tag{176}$$

Then, Equation (173) has the canonical form

$$e^u\left(u - u_+(\alpha)\right)\left(u - u_-(\alpha)\right) = K_{\text{int}}^{(2)}(\alpha), \tag{177}$$

and on the exceptional curve the corresponding approximation is

$$u_{\text{int}} \approx W\left(u_+(\alpha), u_-(\alpha);\, K_{\text{int}}^{(2)}(\alpha)\right), \qquad x_{\text{int}} \approx \delta_{\text{exc}}(\alpha) + \frac{u_{\text{int}}}{2\alpha}. \tag{178}$$

An analytic LIM approximation then follows from Equation (162) by evaluating p_+ at the same point. Outside the exceptional curve (170), this gives the third-order generalized Lambert W_3 approximation; on the exceptional curve, the corresponding quadratic degeneration is used instead.

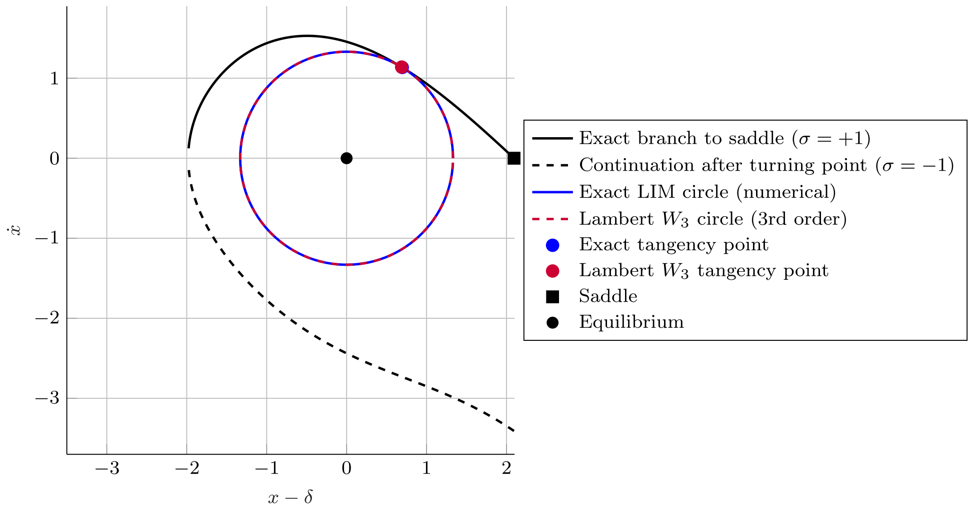

FIGURE 19 | Saddle separatrix and LIM in the tilted periodic potential for $\alpha = 0.2$ and $F = 0.5$. The solid black curve is the exact separatrix branch on the $\sigma = +1$ segment approaching the neighboring saddle, while the dashed black curve shows its continuation after the turning point on the $\sigma = -1$ segment. The blue circle is the numerically determined largest disk centered at the stable equilibrium that remains inside the basin (exact LIM), and the red dashed circle is the third-order generalized Lambert W_3 approximation. Markers indicate the exact and approximate tangency points, the saddle, and the equilibrium.

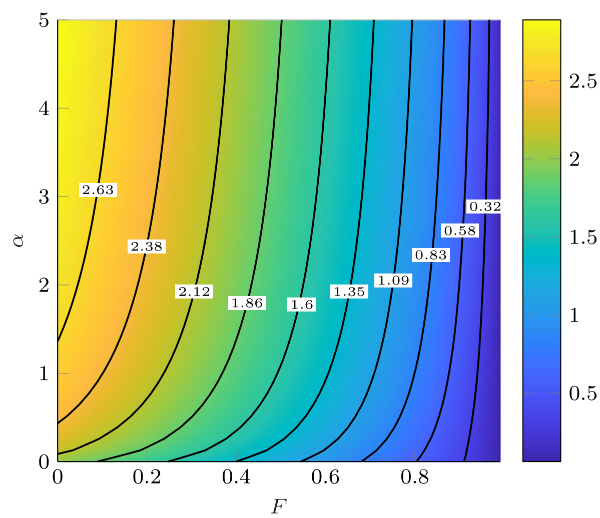

FIGURE 20 | Numerically computed LIM $r_{\mathrm{loc}}(\alpha, F)$ for the washboard potential ($|F| < 1$) over the (F, α) parameter plane. The surface coloring shows the LIM magnitude and the contour lines indicate iso-levels of r_{loc}.

An analytic LIM approximation then follows from Equation (162) by evaluating p_+ at the same point. Figure 19 illustrates, for a representative parameter set $(\alpha, F) = (0.2, 0.5)$, the saddle separatrix that bounds the basin of attraction of the stable equilibrium together with the corresponding LIM. The numerical LIM disk (blue) is obtained as the largest circle centered at $(\delta, 0)$ that remains inside the basin and is tangent to the separatrix; the generalized Lambert W_3 construction (red dashed) provides a closed-form third-order approximation of the same tangency geometry and captures the LIM radius with good accuracy.

To quantify how the basin robustness changes across parameters, Figure 20 reports the numerically computed LIM $r_{\mathrm{loc}}(\alpha, F)$ over the (F, α) plane for $|F| < 1$. As expected, the LIM decreases as the tilt F increases (shallower barriers) and grows with stronger quadratic damping α (enhanced capture), with iso-contours providing a compact map of constant robustness levels.

The accuracy of the third-order generalized Lambert W_3 approximation is summarized in Figure 21, which shows the signed relative error over the same (F, α) domain. The plot identifies parameter regions in which the approximation

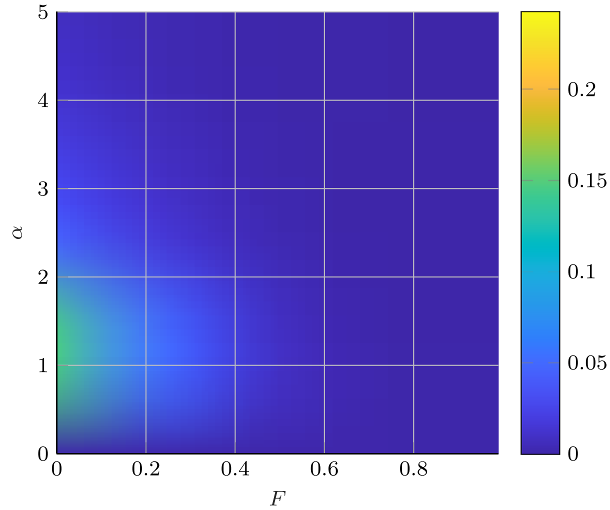

FIGURE 21 | Signed relative error of the generalized Lambert W_3 approximation for the LIM in the washboard potential, plotted over the (F, α) parameter plane. The surface coloring encodes $\left(r_{\text{loc}}^{\text{LW}} - r_{\text{loc}}^{\text{num}}\right)/r_{\text{loc}}^{\text{num}}$ (in percent) and the contour lines indicate iso-levels of the error.

slightly overestimates the true LIM, and it confirms that the approximation is most reliable when either F or α is large. However, even in the worst case, the inaccuracy is about 0.2%.

7 | Conclusions

This paper provides an explicit phase-plane description for autonomous one-degree-of-freedom systems with quadratic air drag and (possibly nonsmooth) Coulomb friction, with a focus on pendulum-type periodic potentials. The central tool is the branchwise substitution $p(x) = \dot{x}^2$ on trajectory segments with fixed velocity sign, a standard transformation in this class of problems, which we apply here. On each such branch, the dynamics reduces to a first-order linear ODE for p as a function of x, yielding closed or semi-closed expressions for phase trajectories, turning points, and, most importantly, separatrix-type curves that partition initial conditions by their long-time outcome.

For the cosine potential with pure quadratic drag, the branchwise construction yields analytic expressions for the saddle-separatrix branches. These curves act as sharp thresholds for barrier crossing, and they induce a winding-number classification of rotational outcomes through an ordered family of critical-velocity stripes in the space of initial conditions (each stripe corresponding to a fixed number of full turns before capture). Moreover, the LIM of the attracting regime around the stable equilibrium can be formulated as a distance-to-boundary problem and reduced to a single scalar tangency condition. Importantly, this reduced tangency equation is numerically easier to solve for the LIM than performing a brute-force computation in the original second-order system. While the tangency location does not admit an elementary closed form, we derive several practical analytic approximations (small-α asymptotics, Lambert W type formulas, and large-α expansion), and we benchmark their accuracy against the direct numerical root solution of the tangency condition.

Adding constant Coulomb friction changes the qualitative picture through set-valued behavior at $\dot{x} = 0$. Besides the usual capture in a well, trajectories can terminate by sticking near the saddle once the restoring torque falls below the friction threshold. This produces sticking intervals and corresponding sticking ribbons in the phase plane. Their boundaries follow from the same branchwise p-construction by prescribing the first turning point at the edge of the sticking band. The LIM becomes piecewise: for moderate friction, the closest boundary point is an interior tangency on the ribbon, whereas for sufficiently large friction, the minimum is attained at the ribbon endpoint, yielding a simple closed-form expression that depends only on the sticking band width.

For normal-force-dependent Coulomb friction, the model remains amenable to the $p(x)$ reduction, but the friction term introduces an additional switching mechanism governed by the curve $p + \cos x = 0$. This necessitates a region-wise linear formulation and a piecewise explicit ribbon boundary with a numerically determined switch point. In this setting, we provided a numerical characterization of the LIM over the (α, μ) parameter plane and identified how the minimizer migrates between the two regions as parameters vary. The outcome highlights a realistic limitation: once friction depends on the state through the normal force, fully closed-form basin boundaries are generally unavailable, yet the construction still organizes the problem into explicit pieces plus a single matching condition.

Finally, for the tilted periodic (washboard) potential with quadratic drag, we obtained closed-form branch trajectories and an explicit criterion separating pinned (capture) dynamics from running (unbounded transport). The key quantity is the minimum of the periodic particular solution $A_+^{(F)}(x)$, which yields a sharp critical damping level $\alpha_{\mathrm{crit}}(F) = F/(2\sqrt{1-F^2})$ for $0 < F < 1$. Below this threshold, a running attractor exists, and trajectories in its basin cross infinitely many barriers, while above it, turning points and capture become unavoidable.

Limitations and outlook. The branchwise reduction $p(x) = \dot{x}^2$ yields explicit phase-plane geometry, but it does not, in general, provide an explicit time parametrization; time-to-event quantities therefore still require time quadratures or numerical integration. For friction laws with additional state-dependent switching (e.g., normal-force-dependent Coulomb friction and sticking), the basin boundaries are only piecewise explicit, and the remaining matching conditions must be solved numerically. Natural extensions include: (i) unbounded potentials such as the Pöschl–Teller potential [59], central-field problems, and the Morse potential [60]; (ii) further spatially varying drag and friction laws with coefficients $\alpha(x)$ and/or $\beta(x)$, such as the modified Van der Pol oscillator or altitude dependent air drag in planetary atmospheres; (iii) non-quadratic damping laws of the form $D(\dot{x}) \sim \alpha\ \mathrm{sgn}(\dot{x})|\dot{x}|^{\gamma}$, for which the same substitution reduces the dynamics to a first-order (generally nonlinear) ODE that may remain analytically tractable; and (iv) clarifying whether analogous order-reduction ideas extend to multi-degree-of-freedom systems, and, if so, identifying the classes of equations of motion for which the resulting reduced equations remain tractable. In these directions, the explicit autonomous results obtained here provide reference cases and building blocks for approximations, including forced or slowly time-varying settings where separatrix splitting becomes relevant.

Acknowledgments

The authors acknowledge the assistance of the following AI tools: OpenAI's ChatGPT (language editing and coding), Grammarly (language editing), and Writefull (language editing).

Open access funding enabled and organized by Projekt DEAL.

Funding

This research was funded by the Deutsche Forschungsgemeinschaft (DFG, German Research Foundation) under Project Number 508244284 and by Israel Science Foundation (grant 3085/25). The authors gratefully acknowledge this support.

Conflicts of Interest

The authors declare no conflicts of interest.

Data Availability Statement

The authors have nothing to report.

References

1. J. F. Dalzell, "A Note on the Form of Ship Roll Damping," *Journal of Ship Research* 22, no. 3 (1978): 178–185.

2. A. Cardo, A. Francescutto, and R. Nabergoj, "On Damping Models in Free and Forced Rolling Motion," *Ocean Engineering* 9 (1982): 171–179.

3. D. W. Bass and M. R. Haddara, "Nonlinear Models of Ship Roll Damping," *International Shipbuilding Progress* 35, no. 401 (1988): 5–24.

4. M. A. S. Neves, N. A. Pérez, and L. Valerio, "Stability of Small Fishing Vessels in Longitudinal Waves," *Ocean Engineering* 26 (1999): 1389–1419.

5. M. Taylan, "The Effect of nonlinear Damping and Restoring in Ship Rolling," *Ocean Engineering* 27 (2000): 921–932.

6. D. Simmonds, "The Response of a Simple Pendulum With Newtonian Damping," *Journal of Sound and Vibration* 84, no. 3 (1982): 453–461.

7. C. E. Mungan and T. C. Lipscombe, "Oscillations of a Quadratically Damped Pendulum," *European Journal of Physics* 34, no. 5 (2013): 1243–1253.

8. J. W. Liang and B. F. Feeny, "Balancing Energy to Estimate Damping Parameters in Forced Oscillators," *Journal of Sound and Vibration* 295, no. 3–5 (2006): 988–998.

9. J. W. Lee, H. W. Kim, H. C. Ku, and W. S. Yoo, "Comparison of External Damping Models in a large Deformation Problem," *Journal of Sound and Vibration* 325, no. 4-5 (2009): 722–741.

10. R. Hauko and R. Repnik, "Damped Harmonic Oscillation: Linear or Quadratic Drag force?" *American Journal of Physics* 87, no. 11 (2019): 910–914.

11. C. R. J. Wylie, "Simple Harmonic Motion With Quadratic Damping," *American Mathematical Monthly* 47, no. 7 (1940): 474–476.

12. K. Klotter, "Free Oscillations of Systems Having Quadratic Damping and Arbitrary Restoring Forces," *Journal of Applied Mechanics* 22, no. 4 (1955): 493–499.

13. P. D. Richardson, "Free Oscillations With Damping Proportional to the Square of the Velocity," *Applied Scientific Research, Section A* 11, no. 4–6 (1963): 397–400.

14. N. N. Bogoliubov and Y. A. Mitropolskii, *Asymptotic Methods in the Theory of Nonlinear Oscillations* (Gordon and Breach, 1961).

15. A. A. Andronov, A. A. Vitt, and S. E. Khaikin, *Theory of Oscillators* (Pergamon Press, 1966).

16. A. H. Nayfeh and D. T. Mook, *Nonlinear Oscillations* (Wiley, 1979).

17. L. Cvetičanin, "Oscillator With Strong Quadratic Damping Force," *Publications de l'Institut Mathématique (Beograd) (NS)* 85, no. 99 (2009): 119–130.

18. I. Kovačič and Z. Rakaric, "Study of Oscillators With a Non-Negative Real-Power Restoring Force and Quadratic Damping," *Nonlinear Dynamics* 64, no. 3 (2011): 293–304.

19. Z. Rakarić and I. Kovačić, "Energy Analysis of Duffing Oscillators With Quadratic Damping: Exact Solutions," *Journal of Physics: Conference Series* 2090 (2021): 012008.

20. A. Chiellini, "Sull'integrazione dell'equazione differenziale $y' + p(x)y + q(x)y^n = 0$," *Bollettino dell'Unione Matematica Italiana* 10 (1931): 301–307.

21. A. Pandey, A. Ghose-Choudhury, and P. Guha, "Chiellini Integrability and Quadratically Damped Oscillators," *International Journal of Non-Linear Mechanics* 92 (2017): 153–159.

22. D. A. Takahashi, "Newton's Equation of Motion With Quadratic Drag Force and Toda's Potential as a Solvable One," *Physica Scripta* 93, no. 7 (2018): 075204.

23. S. Ray and J. Fröhlich, "An Analytic Solution to the Equations of the Motion of a Point Mass With Quadratic Resistance and Generalizations," *Archive of Applied Mechanics* 85, no. 4 (2015): 395–414.

24. K. Yabushita, M. Yamashita, and K. Tsuboi, "An Analytic Solution of Projectile Motion With the Quadratic Resistance Law Using the Homotopy Analysis Method," *Journal of Physics A: Mathematical and Theoretical* 40, no. 29 (2007): 8403–8416.

25. G. W. Parker, "Projectile Motion With Air Resistance Quadratic in the Speed," *American Journal of Physics* 45, no. 7 (1977): 606–610.

26. N. Tsuboi, "On the Optimum Angle of Takeoff in Long Jump," *Transactions of the Japan Society for Industrial and Applied Mathematics* 6 (1996): 393–403.

27. I. Newton, *Philosophiæ Naturalis Principia Mathematica*, 1st ed. (S. Pepys, 1687).

28. J. Bernoulli, "Responsio ad Nonneminis Provocationem, Ejusque Solutio Quaestionis Ipsi Ab Eodem Propositae, De Invenienda Linea Curva Quam Describit Projectile in Medio Resistente," *Acta Eruditorum* 38 (1719): 216–226.

29. L. Euler, *Neue Grundsätze der Artillerie, ins besondere in Ansehung des Widerstands der Luft nebst einem Anhange von den Eigenschaften des Pulvers, und den Wirkungen des Schießpulvers* (A. Haude, 1745), german translation (with additions) of Benjamin Robins'*New Principles of Gunnery*.

30. J. H. Lambert, "Von der Bewegung der Körper in widerstehenden Mitteln," in *Beyträge zum Gebrauche der Mathematik und deren Anwendung*, Vol. 3 (Haude und Spener, 1767), 102–188.

31. J.-C. Borda, "Sur la courbe décrite par les boulets et les bombes, en ayant égard à la résistance de l'air," in *Mémoires de mathématique et de physique de l'Académie royale des sciences* (Imprimerie Royale, 1772), 247–271.

32. A.-M. Legendre, *Dissertation sur la question de balistique proposée par l'Académie Royale des Sciences* (Decker, 1782).

33. I. Didion, *Traité de balistique*, 2nd ed. (Mallet-Bachelier, 1860).

34. H. Lamb, *Dynamics*, 2nd ed. (Cambridge University Press, 1923).

35. W. W. Hackborn, "Projectile Motion: Resistance is Fertile," *American Mathematical Monthly* 115, no. 9 (2008): 813–819.

36. W. W. Hackborn, "On Motion in a Resisting Medium: A Historical Perspective," *American Journal of Physics* 84, no. 2 (2016): 127–134.

37. M. V. Lubarda and V. A. Lubarda, "An Analysis of Pendulum Motion in the Presence of Quadratic and Linear Drag," *European Journal of Physics* 42, no. 5 (2021): 055014.

38. X.-J. Wang, C. Schmitt, and M. G. Payne, "Oscillations With Three Damping Effects," *European Journal of Physics* 23, no. 2 (2002): 155–164.

39. K. K. Likharev, *Dynamics of Josephson Junctions and Circuits* (Gordon and Breach Science Publishers, 1986).

40. J. Clarke and G. Schön, "Macroscopic Quantum Phenomena in Josephson Elements," *Europhysics News* 17, no. 7-8 (1986): 94–96.

41. N. Kyurkchiev, T. Zaevski, A. Iliev, V. Kyurkchiev, and A. Rahnev, "One More Thing on the Subject: Prediction of Chaos in a Josephson Junction With Quadratic Damping by the Melnikov Technique, Possible Probabilistic Control Over Oscillations," *Applied Sciences* 15, no. 23 (2025): 12359.

42. M. S. Soliman and J. M. T. Thompson, "The Effect of Damping on the Steady State and Basin Bifurcation Patterns of a Nonlinear Mechanical Oscillator," *International Journal of Bifurcation and Chaos* 2, no. 1 (1992): 81–91.

43. J. Zhong and S. D. Ross, "Geometry of Escape and Transition Dynamics in the Presence of Dissipative and Gyroscopic Forces in Two Degree of Freedom Systems," *Communications in Nonlinear Science and Numerical Simulation* 82 (2020): 105033.

44. A. Margheri and M. Misquero, "A Dissipative Kepler Problem With a Family of Singular Drags," *Celestial Mechanics and Dynamical Astronomy* 132, no. 3 (2020): 17.

45. M. S. Soliman and J. M. T. Thompson, "Integrity Measures Quantifying the Erosion of Smooth and Fractal Basins of Attraction," *Journal of Sound and Vibration* 135, no. 3 (1989): 453–475.

46. M. S. Soliman and J. M. T. Thompson, "Stochastic Penetration of Smooth and Fractal Basin Boundaries Under Noise Excitation," *Dynamics and Stability of Systems* 5, no. 4 (1990): 281–298.

47. S. Lenci, G. Rega, and L. Ruzziconi, "The Dynamical Integrity Concept for Interpreting/Predicting Experimental Behaviour: From Macro- to Nano-Mechanics," *Philosophical Transactions of the Royal Society A: Mathematical, Physical and Engineering Sciences* 371, no. 1993 (2013): 20120423.

48. G. Rega and S. Lenci, "Identifying, Evaluating, and Controlling Dynamical Integrity Measures in Non-Linear Mechanical Oscillators," *Nonlinear Analysis: Theory, Methods & Applications* 63, no. 5–7 (2005): 902–914.

49. M. Leszczyński, P. Perlikowski, T. Burzyński, T. M. Kowalski, and P. Brzeski, "Review of Sample-Based Methods Used in an Analysis of Multistable Dynamical Systems," *Chaos* 32, no. 8 (2022): 082101.

50. G. Habib, "Dynamical Integrity Assessment of Stable Equilibria: A New Rapid Iterative Procedure," *Nonlinear Dynamics* 106 (2021): 2073–2096.

51. D. Patkó and G. Habib, "Dynamical Integrity of Periodic Orbits: A Computationally Efficient Approach," *Nonlinear Dynamics* 113 (2025): 24641–24661.

52. A. Genda, A. Fidlin, and O. V. Gendelman, "Basins of Attraction and Dynamic Integrity in 1-dof Autonomous Systems With Quadratic Drag," preprint, Research Square, February 10, 2026, (Version 1), https://doi.org/10.21203/rs.3.rs-8774429/v1.

53. I. Mező and Á. Baricz, "On the Generalization of the Lambert W Function With Applications in Theoretical Physics," preprint, arXiv, June 22, 2015, version 2, https://doi.org/10.48550/arXiv.1408.3999.

54. I. Mező and Á. Baricz, "On the Generalization of the Lambert W Function," *Transactions of the American Mathematical Society* 369, no. 11 (2017): 7917–7934.

55. A. I. Neishtadt, A. A. Vasiliev, and A. V. Artemyev, "Capture Into Resonance and Escape From It in a Forced Nonlinear Pendulum," *Regular and Chaotic Dynamics* 18, no. 6 (2013): 686–696.

56. A. I. Neishtadt, "Averaging, Passage Through Resonances, and Capture Into Resonance in Two-Frequency Systems," *Russian Mathematical Surveys* 69, no. 5 (2014): 771–843.

57. J. Fajans and L. Friedland, "Autoresonant (Nonstationary) Excitation of Pendulums, Plutinos, Plasmas, and Other Nonlinear Oscillators," *American Journal of Physics* 69, no. 10 (2001): 1096–1102.

58. L. Friedland, "Efficient Capture of Nonlinear Oscillations Into Resonance," *Journal of Physics A: Mathematical and Theoretical* 41, no. 41 (2008): 415101.

59. T. Pöschl, "Zur frage der Schwingungen nach dem quadratischen Widerstandskraftgesetz," *Physikalische Zeitschrift* 29 (1928): 938.

60. P. M. Morse, "Diatomic Molecules According to the Wave Mechanics. II. Vibrational Levels," *Physical Review* 34 (1929): 57–64.